Chapter

High-Entropy Superconducting Materials

Pablo Cayado and Jens Hänisch

Abstract

High-entropy alloys are a rapidly evolving field of materials research and have gained increasing attention in recent years. Characterized by their multicomponent compositions, they were originally created by mixing a multitude of metallic elements and expanded the idea of traditional alloy design, opening new paths for materials research. In particular, the discoveries of superconductivity in some of these alloys since 2014 provided a new impetus for exploring novel superconducting phenomena and materials. In fact, the concept of increasing entropy in superconducting compounds, firstly restricted to alloys or intermetallics, was soon extended to other types of superconductors enriching drastically the research in the field. The high-entropy superconductors are nowadays a matter of intense study. This chapter provides a comprehensive review of the most recent and relevant research on the different types of high-entropy superconductors. The current state of research, synthesis methods, and characterization techniques are included. This information may serve as a reference for future research on this topic and inspire further exploration and innovation in the application of these materials.

Keywords: superconductor, high-entropy alloy, high-entropy ceramic, high-entropy oxide, REBCO

1. Introduction

High-entropy alloys (HEAs) are a category of materials that has attracted attention in recent times in different fields of materials research. This new paradigm for alloy design, proposed around two decades ago [1, 2], consists of multiple species of atoms randomly intermixed, resulting in a notable level of disorder, specifically in high configurational entropy. This severe disorder appears due to the mixing of several atom species in considerable proportions on specific lattice sites.

The definition of a HEA, or, in other words, the difference between HEA and medium-entropy alloys or even the usual low-entropy alloys, is based on the number of elements present in the alloy and their proportions. An alloy is usually called HEA if it contains a mixture of at least five elements, typically in proportions between 5% and 35% [1], although some authors claim that mixtures of four elements may also be considered HEAs [3]. The entropy of such mixtures can be evaluated as:

$$\Delta S_{\mathrm{mix}} = -R \sum_{i=1}^{n} x_i \ln x_i \qquad (1)$$

where x_i is the molar fraction of component i, n is the total number of components, and R = 8.314 J/mol K is the gas constant. An equimolar system with five components has a ΔS_{mix} value of 1.609R, which is also often used as an equivalent, stricter criterion for HEA [4]. In the following, we keep the definition of at least five components taking part in mixing while softening occasionally the criteria of composition and ΔS_{mix}.

The change in entropy lowers the Gibbs energy according to:

$$\Delta G_{\mathrm{mix}} = \Delta H_{\mathrm{mix}} - T\Delta S_{\mathrm{mix}} \qquad (2)$$

with H_{mix} being the mixing enthalpy, which allows the stabilization of disordered compounds into certain singular crystal structures with substantial chemical substitutional disorder, rather than leading to the creation of multiple crystalline phases.

Among all the novel properties that emerged in HEAs, the appearance of superconductivity in some of them is one of the most interesting ones. This was seen for the first time in 2014 in the system $Ta_{34}Nb_{33}Hf_8Zr_{14}Ti_{11}$ [5] with a rather high critical temperature, T_c, of ~7.3 K [5]. This finding was the starting point of intense research into the topic as the combination of superconductivity and superior mechanical properties that HEAs typically gives them some application potential to be evaluated and utilized. Due to the large degree of disorder and hence short electron mean free paths and therefore coherence lengths, all HEA superconductors are type II. Often, their B_{c2} is measured resistively, rarely also their B_{c1} magnetically. Critical current densities are usually not reported with the exception of the REBa$_2$Cu$_3$O$_{7-x}$ (REBCO, RE rare earth elements) compounds. Most HEAs are fabricated by arc melting. In recent years, further preparation methods were investigated, such as solid-state reaction (SSR), spark-plasma sintering, hot-press sintering, and thin-film growth (sputtering, pulsed laser deposition, and chemical solution deposition).

Over the years, the concept of "high-entropy," that is, incorporating multiple components within the same matrix, has been expanded to various types of superconductors like BiS$_2$-based, Van der Waals, rock-salt-type, A15-type, and transition-metal-zirconide (TrZr$_2$)-type superconductors. Most recently, this approach has been further extended to intermetallics as well as compounds containing non-metallic constituents like oxides, carbides, borides, nitrides, and sulfides. Particularly interesting in the field of superconductivity are the high-entropy oxides (HEO), in which the well-known REBCO compounds, probably the superconductors with the largest potential from the applications point of view, are included. The research on HE REBCO has started only few years ago, but it is a topic with promising perspectives. There is considerable variety in stoichiometry notation in literature. We occasionally carefully modified it for better comparability. For the alloys, we adopted 100% notation and (near) equimolar mixes without further subscripts, that is, the number outside of the brackets represents the sum of the chemical compositions of the elements in parentheses, for instance, (TaNb)$_{67}$ refers to $Ta_{1/3}Nb_{1/3}$. Parts in 6 or 7, we note as 1/6 and 1/7 to avoid odd numbers and false accuracy. For the HE compounds, we mostly used the stoichiometry notation of the parent compounds.

1.1 Categorizing

Considering the composition and the structural and physical characteristics of the different HEAs, Sun et al. proposed a first classification by dividing them into four different groups [4]. The group of type A includes HEA superconductors made of metals from the left side of the transition-metal region of the periodic table like the different stoichiometries of the Ta-Nb-Hf-Zr-Ti system and most of the related compounds coming from elemental substitutions such as Nb-Re-Hf-Zr-Ti or Hf-Nb-Ti-V-Zr. These type A HEAs crystallize in bcc lattices and show T_c values between 4.0 K and 9.2 K and a maximum $B_{c2}(0)$ of $\sim$11.7 T. The type B HEA superconductors are mainly composed of early transition metals (groups 3 to 7 of the periodic table), but crystallize in rather complex lattices, which could be large bcc α-Mn-type lattices or smaller bcc and hcp lattices, depending on the stoichiometry. Compounds like $(ZrNb)_{30}(MoReRu)_{70}$, $(HfTaWIr)_{70}Re_{30}$, or $(HfTaWPt)_{50}Re_{50}$ belong to this group. The T_c in this class is usually lower than for type A HEAs with values between 1.9 K and 5.7 K, and the highest known $B_{c2}(0)$ is $\sim$7.9 T. The third group, type C HEA superconductors, crystallizes in a CsCl-type structure and is composed of early transition metals combined with late transition metals, such as the Sc-Zr-Nb-Ta-Rh-Pd system. They show T_c values between 3.9 K and 9.3 K and $B_{c2}(0)$ values up to $\sim$10.7 T. The fourth group, type D HEA superconductors, crystallizes in the hcp structure. Examples are $Re_{56}Nb_{11}Ti_{11}Zr_{11}Hf_{11}$, $(MoReRuRh)_{95}Ti_5$, and Nb_{10+2x} $Mo_{35-x}Ru_{35-x}Rh_{10}Pd_{10}$. This last alloy shows the highest T_c of this class, with a value of 6.19 K for x = 2.5. With the appearance of more and more different types of superconducting high-entropy compounds, this classification was extended by naming them simply according to their crystal structure.

One parameter that may have a great influence on the stability of HEAs is the valence electron count (VEC), which is better expressed as the number of valence electrons per atom in the particular case of HEAs. The VEC reflects the total density of states at the Fermi level and plays a crucial role in determining the T_c of superconductors that follow the Bardeen-Cooper-Schriefer (BCS) theory. In fact, a robust correlation between VEC and T_c is evident in binary and ternary superconducting transition-metal alloys, commonly known as the Matthias rule [6]. In the case of HEAs, there is also a relationship between the VEC and T_c similar to the Matthias rule. In **Figure 1**, the dependence of T_c on the VEC is shown for different types of superconducting HEAs. The type A HEAs that crystallize in bcc structure appear in the VEC range 4.2–4.8, reaching a maximum T_c for a VEC of 4.7. In the case of type C HEAs, with CsCl-type structures, superconductivity emerges in the VEC range of 5.9–6.3, with a maximum T_c at a VEC of $\sim$5.9. These two types of HEAs have similar behavior to the simpler binary alloys with the characteristic two-peak character seen for the near VECs of 4.7 and 5.9. However, the type B HEAs with a more complex α-Mn structure do not follow this general trend. Although the bcc and CsCl crystal structures are closely related to the α-Mn structure, their atomic arrangements differ in a remarkable way, making their stabilities to be limited to narrow ranges of VEC. The type D HEAs, the ones that show hcp structure, show superconducting behavior for VEC values similar to the type C ones. Finally, it is possible to add to this analysis the more recent HEAs. The A15-type HEAs show similar behavior as the binary A15 superconductors that follow the Matthias rule, with VEC falling between 4.55 and 4.85. Also, the σ-phase HEAs resemble their relatives, the binary σ-phase superconductors whose VEC values extend from 6.07 to 6.84 with a T_c maximum at VEC $\sim$ 6.5 in accordance with the Matthias rule [6]. The VECs of the σ-phase HEAs are located at
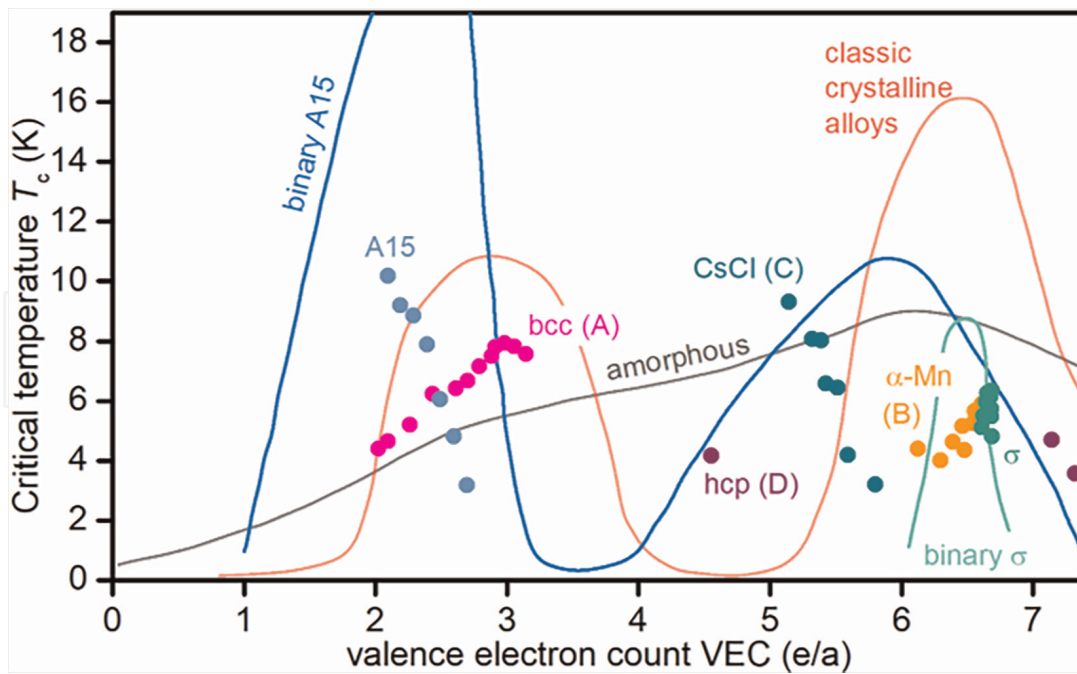
Figure 1.
Dependence of the critical temperature T_c *on the valence electron count (VEC) for different types of high-entropy superconductors. Data extracted from Refs. [4, 7, 8].*

the electron-rich side of this region and are higher than those of most HEA superconductors. Note that the VEC ranges of the σ phase and the α-Mn type HEA superconductors are very close. These dependencies show that the VEC serves as a crucial tool for predicting potential HEA superconductors and can be useful for understanding the superconducting properties of the new systems.

Below, the state of the art of each of these HE superconductor classes will be reported. Special attention will be paid to the superconducting properties of each compound and their prospects for further development.

2. Superconducting high-entropy alloys

2.1 The Ta-Nb-Hf-Zr-Ti system

Superconductivity in high-entropy alloys was first discovered by Koželj et al. in 2014 for a particular stoichiometry of the Ta-Nb-Hf-Zr-Ti system [5]. Investigations on this system had already started years prior due to its superior structural and mechanical properties [9]. Varying the original equimolar ratio of the elements led to the $Ta_{34}Nb_{33}Hf_8Zr_{14}Ti_{11}$ compound that appeared to be superconducting below a critical temperature of ~7.3 K. The original compound was a polycrystalline sample with grains in the range of 2–300 μm fabricated by arc melting. It crystallized in a highly distorted body-centered cubic (bcc) structure (a = 3.36 Å), **Figure 2a**, due to the difference in the atomic radii of the constituent elements. Apart from its ~7.3 K T_c, it shows an upper critical field $B_{c2}(0) \sim 8.2$ T, a lower critical field $B_{c1} \sim 32$ mT, and an energy gap opening of ~2.2 meV. Moreover, first principle calculations showed that it could be classified as a strong electron-phonon coupling superconductor with a coupling constant $\lambda = 1.16$ [11].

This discovery soon caught the attention of several groups, who started to investigate this system, preparing the samples, as in the original work, by an arc melting
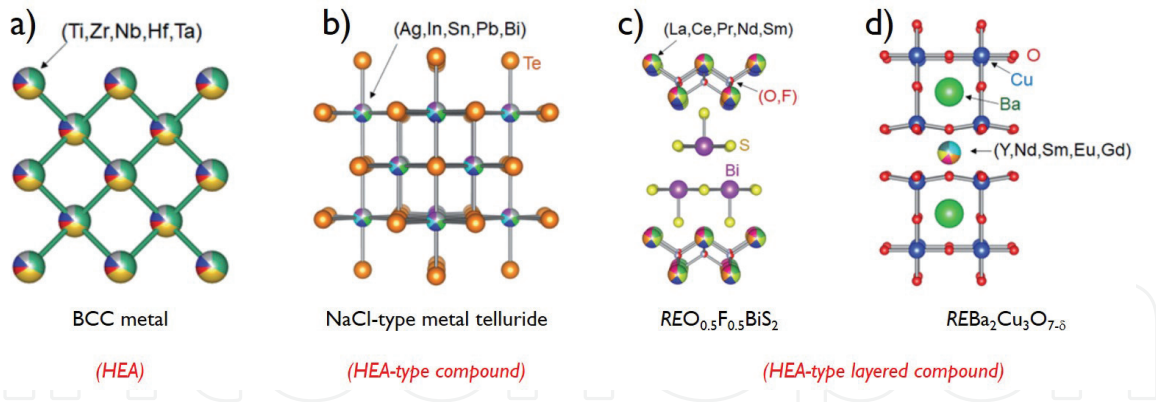
Figure 2.
Crystal structures of several high-entropy superconductors. Reproduced with permission from [10].

method as summarized in **Table 1**. A stoichiometry series, studied a couple of years later by von Rohr et al., was $[\text{TaNb}]_{100-x}(\text{HfZrTi})_x$, where x took 12 different values from 20 to 84 [13]. This study revealed T_c variations between 4.49 K and 7.92 K for the different stoichiometries, with the largest upper critical field of $\sim$11.67 T for the sample with x = 0.5. A particular stoichiometry of this compound, $(\text{TaNb})_{67}(\text{HfZrTi})_{33}$, was further studied by Guo et al. [14] at high pressures, revealing an exceptionally resilient zero-resistance superconductivity under pressures up to 190.6 GPa. In their study, the authors observed that initially, the T_c of this compound rose from 7.7 K at ambient pressure to 10 K at $\sim$60 GPa, followed by a slight, gradual decrease to 9 K at 190.6 GPa, which is close to the pressure in the outer core of the Earth. The authors proposed therefore that this compound is a potential candidate for new applications under extreme pressure conditions. Similar results confirming the robustness of the superconductivity in the Ta-Nb-Hf-Zr-Ti system were obtained by Vrtnik et al. [12], who prepared samples with different numbers of elements (4 and 5) as well as differing stoichiometry (equimolar and off-equimolar) by arc melting and subjected them to different thermal treatments. Their results show that the samples are superconducting independently of the thermal treatment and the resulting micro-structure. In addition, Jasiewicz et al. [19] further investigated the pressure effects on the electronic structure, electron-phonon interaction, and superconductivity of $(\text{TaNb})_{67}(\text{HfZrTi})_{33}$ from 0 to 100 GPa. Their investigation confirmed the previous-ly reported results, observing the same T_c trend with pressure. However, they could also prove that this evolution of T_c with pressure can be well explained in the frame-work of the classical electron-phonon mechanism. A certain variant also investigated was $\text{Ta}_{1/6}\text{Nb}_{2/6}\text{Hf}_{1/6}\text{Zr}_{1/6}\text{Ti}_{1/6}$ by Kim et al. [16]. With a T_c = 7.85 K, it shows a $B_{c1}(0) \sim$ 23 mT and a $B_{c2}(0) \sim$ 12.05 T, a higher value than the one found for the $(\text{TaNb})_{50}(\text{HfZrTi})_{50}$ commented before. This work was the first one to report about critical current density and pinning mechanisms in this type of systems. The authors reported a critical current density (J_c) of $\sim$10.7 kA/cm^2 at 2 K in self-field and found that the pinning mechanism agreed with the double exponential model, which was first introduced for MgB_2 by Horvat et al. [20], indicating that there were two types of pinning mechanism active. Kim et al. [17] investigated recently the effect of vacuum annealing at several temperatures and at different times on the superconducting and mechanical properties of this compound. Even though T_c and B_{c2} slightly decreased upon annealing at medium temperatures (550°C), it had a positive effect on both J_c and Vickers hardness (HV_{IT}). Record values

Nominal composition	T_c (K)	$B_{c1}(0)$ (mT)	$B_{c2}(0)$ (T)	Reference
$Ta_{34}Nb_{33}Hf_8Zr_{14}Ti_{11}$	7.3	32	8.2	[5]
$Ta_{34}Nb_{33}Hf_8Zr_{14}Ti_{11}$	7.8	—	8.15	[12]
$[TaNb]_{70}(ZrHfTi)_{30}$	8.03	—	6.67	[13]
$[TaNb]_{67}(ZrHfTi)_{33}$	7.75	—	7.75	[13]
$[TaNb]_{67}(ZrHfTi)_{33}$	7.7 (1 atm)	—	—	[14]
$[TaNb]_{67}(ZrHfTi)_{33}$	10 (60 GPa)	—	—	[14]
$[TaNb]_{67}(ZrHfTi)_{33}$	9 (190.6 GPa)	—	—	[14]
$[TaNb]_{60}(ZrHfTi)_{40}$	7.56	—	8.43	[13]
$[TaNb]_{50}(ZrHfTi)_{50}$	6.46	—	11.67	[13]
$[TaNb]_{16}(ZrHfTi)_{84}$	4.52	—	9.02	[13]
$Ta_{20}Nb_{21}Hf_{20}Zr_{20}Ti_{19}$	6.9	—	10.45	[12]
$Ta_{20}Nb_{20}Hf_{20}Zr_{20}Ti_{20}$	7.12			[15]
$Ta_{22}Nb_{24}Hf_{21}Zr_{23}Ti_{10}$	6.2	—	—	[12]
$Ta_{1/6}Nb_{2/6}Hf_{1/6}Zr_{1/6}Ti_{1/6}$	7.85	23	12.05	[16]
$Ta_{1/6}Nb_{2/6}Hf_{1/6}Zr_{1/6}Ti_{1/6}$	8.1		11.0	[17]
$Ta_{11}Nb_{34}Hf_8Zr_{14}Ti_{33}$	7.5	15	12.2	[18]

Table 1.
Selected properties of superconducting Ta-Nb-Hf-Zr-Ti HEAs, all prepared by arc melting.

of $J_c(0)$ = 520 kA/cm^2 and HV_{IT} = 528 were reported, an increase of 1860% and 32%, respectively. The best samples of Refs. [16, 17], **Table 1**, investigated are (also) included in **Table 2** for comparison of J_c. The already high value of $B_{c2}(0)$ found in [16] was recently overcome in the $Nb_{34}Ti_{33}Zr_{14}Ta_{11}Hf_8$ alloy with $B_{c2}(0) \sim 12.2$ T, although it has a lower T_c = 7.5 [18]. For a summary of the Ta-Nb-Hf-Zr-Ti HEAs, see **Table 1**.

2.2 Substitutions in Ta-Nb-Hf-Zr-Ti

The natural evolution of the field led to the study of new compositions and mixtures of elements, first by only replacing one of the elements. These compounds, summarized in **Table 3**, crystallize in the bcc structure and belong to type A too. An alternative soon investigated by Marik et al. [27] was the equimolar Nb-Re-Hf-Zr-Ti HEA, the result of substituting Re for Ta in the original system. Prepared by arc melting too, it was among the first equimolar HEA superconductors. With $T_c \sim 5.3$ K, it shows an upper critical field $B_{c2}(0)$ of 8.88 T, a value close to the BCS weak coupling Pauli limit, in contrast to other compounds of the Ta-Nb-Hf-Zr-Ti system [17]. The same elements in different stoichiometry were employed by Motla et al. [28] in the synthesis of $Nb_{60}Re_{10}Zr_{10}Hf_{10}Ti_{10}$. This variant shows a T_c = 5.7 K, and it was studied in detail by means of different electronic characterization techniques, including muon spin relaxation and rotation, finding electronic properties similar to conventional binary and ternary superconducting compounds, that is, s-wave symmetry of the order parameter and phonon-mediated pairing [18]. Ta was also substituted by Mo in the equimolar HfMoNbTiZr, resulting in T_c = 4.1 K and $B_{c2}(0)$ = 5.55 T [30]. Re, on

Nominal composition	Synthesis method	T_c (K)	$B_{c2}(0)$ (T)	J_c (kA/cm^2)	Reference
Ta$_{1/6}$Nb$_{2/6}$Hf$_{1/6}$Zr$_{1/6}$Ti$_{1/6}$	Arc melting	7.85	12.05	10.7 (2 K, sf)	[16]
Ta$_{1/6}$Nb$_{2/6}$Hf$_{1/6}$Zr$_{1/6}$Ti$_{1/6}$	Arc melting	8.1	11	520 (4 K, sf)	[17]
Ta$_{1/6}$Nb$_{2/6}$Hf$_{1/6}$Zr$_{1/6}$Ti$_{1/6}$	SPS	7.80	10.50	30.5 (2 K, 0.01 T) 73.2 (4 K, 0.01 T)	[21]
Ta$_{1/6}$Nb$_{2/6}$Hf$_{1/6}$Zr$_{1/6}$Ti$_{1/6}$	Hot-press sintering	7.90	—	—	[22]
Ta$_{1/6}$Nb$_{2/6}$Hf$_{1/6}$Zr$_{1/6}$Ti$_{1/6}$	PLD	7.28	12.10	1.8 (4.2 K, sf)	[23]
(TaNb)$_{12}$(HfZrTi)$_{88}$	Sputtering	2.77	6.15	—	[24]
(TaNb)$_{24}$(HfZrTi)$_{76}$	Sputtering	4.61	10.44	—	[24]
(TaNb)$_{35}$(HfZrTi)$_{65}$	Sputtering	5.60	11.05	—	[24]
(TaNb)$_{46}$(HfZrTi)$_{54}$	Sputtering	6.14	9.93	—	[24]
(TaNb)$_{57}$(HfZrTi)$_{43}$	Sputtering	6.76	8.77	—	[24]
(TaNb)$_{67}$(HfZrTi)$_{33}$	Sputtering	6.43	7.05	—	[24]
(TaNb)$_{79}$(HfZrTi)$_{21}$	Sputtering	6.33	5.78	—	[24]
(TaNb)$_{87}$(HfZrTi)$_{13}$	Sputtering	6.02	4.29	—	[24]
(TaNb)$_{96}$(HfZrTi)$_{04}$	Sputtering	5.57	2.95	—	[24]
(TaNb)$_{70}$(HfZrTi)$_{30}$ (600 nm)	Sputtering	5.31	5.80	—	[25]
(TaNb)$_{70}$(HfZrTi)$_{30}$ (100 nm)	Sputtering	2.69	3.20	—	[25]
(TaNbZrTi)$_{90}$W$_{10}$	Sputtering	6.20	—	—	[26]
(TaNbZrTi)$_{90}$V$_{10}$	Sputtering	6.20	—	—	[26]

Table 2.
Selected properties of superconducting Ta-Nb-Hf-Zr-Ti HEAs prepared by methods different from the conventional arc melting.

the other hand, was also used by Hattori et al. [29] to substitute not the Ta but the Zr, leading to the Ti-Hf-Nb-Ta-Re system. Different stoichiometries with VEC values ranging from 4.6 to 5.0 were investigated, finding T_c values between 3.25 K and 4.38 K and $B_{c2}(0)$ values between 7.90 T and 5.91 T, with the maximum T_c occurring for a VEC of 4.7 and the maximum $B_{c2}(0)$ for a VEC of 4.6 [27]. The Zr was also substituted, in this case by Mo by Zeng et al. [31], to prepare equimolar TiHfNbTaMo samples that showed a T_c = 3.42 K and $B_{c2}(0)$ = 3.95 T [28]. The Zr was also replaced by V in the equimolar HfNbTaTiV HEA [34]. The detailed characterization determined T_c = 5.0 K, B_{c1} = 19 mT and $B_{c2}(0)$ = 6.63 T [30]. Another substitution, V for Ta, led to Hf$_{21}$Nb$_{25}$Ti$_{15}$V$_{15}$Zr$_{24}$, which shows a T_c value of 5.3 K [33]. In the case of [TaNb]$_{31}$(TiUHf)$_{69}$, the substitution was U for Zr [35]. This was the first HEA containing an *f*-electron element, and it extended the HEA research to actinide elements, opening the possibility of leveraging HEAs as functional waste forms for a variety of radioisotopes. This system shows phonon-mediated superconductivity with $T_c \sim 3.2$ K and $B_{c2}(0) \sim 6.4$ T [31].

Other elemental substitutions of two or more elements in the Ta-Nb-Hf-Zr-Ti system were studied by von Rohr et al. [36] with systematic isoelectronic replacements, using Mo-Y, Mo-Sc, and Cr-Sc mixtures and also adding Al to the initial

Nominal composition	T_c (K)	$B_{c1}(0)$ (mT)	$B_{c2}(0)$ (T)	Reference
$Re_{20}Nb_{20}Hf_{20}Zr_{20}Ti_{20}$	5.3	33	8.88	[27]
$Re_{10}Nb_{60}Hf_{10}Zr_{10}Ti_{10}$	5.7	7.95	6.31	[28]
$Ta_5Nb_{25}Hf_{25}Re_{10}Ti_{35}$	3.95	4.87	7.90	[29]
$Ta_5Nb_{35}Hf_{20}Re_{10}Ti_{30}$	4.38	6.60	6.94	[29]
$Ta_{15}Nb_{35}Hf_{15}Re_{10}Ti_{25}$	4.10	4.56	6.65	[29]
$Ta_{25}Nb_{35}Hf_{10}Re_{10}Ti_{20}$	3.62	7.15	5.85	[29]
$Ta_{35}Nb_{35}Hf_5Re_{10}Ti_{15}$	3.25	6.87	5.91	[29]
$Mo_{20}Nb_{20}Hf_{20}Zr_{20}Ti_{20}$	4.1	5.2	5.82	[30]
$Ta_{20}Nb_{20}Hf_{20}Mo_{20}Ti_{20}$	3.42	22.8	3.95	[31]
$(TaNb)_{0.67}(HfMoW)_{0.33}$	4.3	—	1.45	[32]
$V_{15}Nb_{25}Hf_{21}Zr_{24}Ti_{15}$	5.30	—	—	[33]
$Ta_{20}Nb_{20}Hf_{20}V_{20}Ti_{20}$	4.93	—	6.63	[34]
$[TaNb]_{31}(HfUTi)_{69}$	3.20	—	6.40	[35]
$[\{Sc_{33}Cr_{67}\}Nb]_{67}(HfZrTi)_{33}$	5.60	—	—	[36]
$[Ta\{Sc_{33}Cr_{67}\}]_{67}(HfZrTi)_{33}$	4.40	—	—	[36]
$[TaNb]_{67}(\{Sc_{67}Cr_{33}\}ZrTi)_{33}$	7.50	—	—	[36]
$[TaNb]_{67}(Hf\{Sc_{67}Cr_{33}\}Ti)_{33}$	7.40	—	—	[36]
$[TaNb]_{67}(HfZr\{Sc_{67}Cr_{33}\})_{33}$	7.60	—	—	[36]
$[\{Y_{33}Mo_{67}\}Nb]_{67}(HfZrTi)_{33}$	4.70	—	—	[36]
$[Ta\{Y_{33}Mo_{67}\}]_{67}(HfZrTi)_{33}$	3.50	—	—	[36]
$[TaNb]_{67}(\{Y_{67}Mo_{33}\}ZrTi)_{33}$	7.60	—	—	[36]
$[TaNb]_{67}(Hf\{Y_{67}Mo_{33}\}Ti)_{33}$	6.70	—	—	[36]
$[TaNb]_{67}(HfZr\{Y_{67}Mo_{33}\})_{33}$	7.50	—	—	[36]
$[\{Sc_{33}Mo_{67}\}Nb]_{67}(HfZrTi)_{33}$	4.40	—	—	[36]
$[Ta\{Sc_{33}Mo_{67}\}]_{67}(HfZrTi)_{33}$	2.90	—	—	[36]
$[TaNb]_{67}(\{Sc_{67}Mo_{33}\}ZrTi)_{33}$	7.50	—	—	[36]
$[TaNb]_{67}(Hf\{Sc_{67}Mo_{33}\}Ti)_{33}$	6.60	—	—	[36]
$[TaNb]_{67}(HfZr\{Sc_{67}Mo_{33}\})_{33}$	7.50	—	—	[36]
$Ta_{20}Nb_{20}Fe_{20}Zr_{20}Ti_{20}$	6.87	—	—	[15]
$Ta_{20}Nb_{20}Ge_{20}Zr_{20}Ti_{20}$	8.46	—	—	[15]
$Ta_{1/6}Nb_{1/6}Hf_{1/6}Zr_{1/6}Ti_{1/6}V_{1/6}$	5.09	—	—	[15]
$Ta_{1/6}Nb_{1/6}Ge_{1/6}V_{1/6}Zr_{1/6}Ti_{1/6}$	8.40	—	—	[15]
$Ta_{1/6}Nb_{1/6}Si_{1/6}V_{1/6}Zr_{1/6}Ti_{1/6}$	4.29	—	—	[15]
$Ta_{1/6}Nb_{1/6}Si_{1/6}Ge_{1/6}Zr_{1/6}Ti_{1/6}$	7.40	—	—	[15]
$Ta_{20}Nb_{20}Hf_{20}Sc_{20}Ti_{20}$	6.60	—	13.10	[37]
$Ta_{20}Nb_{20}Hf_{20}Zr_{20}Sc_{20}$	7.70	—	12.40	[37]
$Ta_{20}Nb_{20}Sc_{20}Zr_{20}Ti_{20}$	7.90	—	19.30	[37]
$Ta_{1/6}Nb_{1/6}Hf_{1/6}Zr_{1/6}Ti_{1/6}Sc_{1/6}$	7.20	—	14.10	[37]

Nominal composition	T_c (K)	$B_{c1}(0)$ (mT)	$B_{c2}(0)$ (T)	Reference
Al$_{15}$Nb$_{24}$V$_5$Zr$_{26}$Ti$_{40}$	5.36	—	—	[38]
Al$_{15}$Nb$_{14}$V$_5$Zr$_{41}$Ti$_{35}$	4.73	—	—	[38]
Al$_{15}$Nb$_{24}$V$_5$Zr$_{31}$Ti$_{35}$	5.45	—	—	[38]
Al$_{15}$Nb$_{34}$V$_5$Zr$_{21}$Ti$_{35}$	6.47	—	—	[38]
Al$_{15}$Nb$_{44}$V$_5$Zr$_{11}$Ti$_{35}$	6.75	—	—	[38]
Al$_{15}$Nb$_{14}$V$_5$Zr$_{31}$Ti$_{45}$	4.96	—	—	[38]
Al$_{15}$Nb$_{34}$V$_5$Zr$_{31}$Ti$_{25}$	6.18	—	—	[38]
Al$_{15}$Nb$_{44}$V$_5$Zr$_{31}$Ti$_{15}$	6.98	—	—	[38]

Table 3.
Selected properties of superconducting type A Ta-Nb-Hf-Zr-Ti-based HEAs with different substitutions (bold). All samples are prepared by arc melting.

[TaNb]$_{67}$(HfZrTi)$_{33}$ compound ([TaNb]$_{67}$(HfZrTi)$_{33}$Al$_x$). This study concluded that T_c strongly depends on the elemental composition of the alloy. This change is clearly visible when substituting Nb and also Ta, observing a 60% decay in T_c of [Ta {Sc$_{33}$Mo$_{67}$}]$_{67}$(HfZrTi)$_{33}$. The replacement of the other three metals does not change T_c so drastically, which remains almost unchanged for the replacement of Hf and Ti and being ∼1 K lower for the replacement of Zr. In the case of the Al addition, an improvement of the crystallinity of the compounds was realized until $x = 40$, when the stabilization of a simple bcc lattice breaks down and the material starts to crystallize in the β-uranium structure, resulting in a suppression of superconductivity below 1.8 K [34]. Similar conclusions can be extracted from the work of Wu et al. [15], who added Fe, Ge, Hf, Si, and/or V instead of Hf to the original NbTaTiZr-based matrix. The analysis of the physical properties of the prepared compounds, including up to seven elements, revealed that the superconducting behavior varies with the composition distribution of Nb+Ta and the degree of lattice distortion generated by the change in the total number of elements. As the number of elements increases from four to seven, the Nb+Ta content reduces, causing a decrease in T_c [20]. The addition of Sc to the NbTaTiZr-based matrix generates a two-phase structure, with one phase being bcc, very similar to the Hf-Nb-Ta-Ti-Zr parent system and the other one hcp, which absorbs practically all Sc. Superconductivity emerges in the bcc phase with $T_c = 7.2$ K and $B_{c2}(0) = 14.1$ T, very similar to the Hf-Nb-Ta-Ti-Zr parent alloys [37]. Another studied system was Al-Nb-Ti-V-Zr. Harayama et al. [39] prepared Al$_5$Nb$_x$Ti$_{35}$V$_5$Zr$_{55-x}$ and Al$_5$Nb$_x$Ti$_{59-x}$V$_5$Zr$_{31}$ samples, including the particular composition Al$_5$Nb$_{24}$Ti$_{40}$V$_5$Zr$_{26}$, which have an interesting gum-metal-like behavior characterized by being superelastic and having a low Young's modulus [35]. The T_c values of these compounds vary from 5.36 K to 7.01 K, being the maximum for the Al$_5$Nb$_{44}$Ti$_{15}$V$_5$Zr$_{31}$ sample, following the T_c dependence on the VEC typical for the bcc-type HEA superconductors of type A [38]. The (TaNb)$_{67}$(HfMoW)$_{33}$ HEA was also investigated in detail. This HEA exhibits a metallic behavior at high temperature, while at $T_c \sim 4.3$ K, it becomes superconducting with an upper critical field $B_{c2}(0) \sim 1.45$ T [32].

2.3 Preparation methods

Until recent times, superconducting HEAs were generally prepared by arc melting. In the search for new features, alternative preparation methods were started,

summarized in **Table 2**. Some of them, like Spark-Plasma Sintering (SPS) employed to synthesize $Ta_{1/6}Nb_{2/6}Hf_{1/6}Zr_{1/6}Ti_{1/6}$ samples, serve to obtain bulk samples similar to those prepared by arc melting. The T_c = 7.8 K and $B_{c2}(0)$ = 10.5 T of these samples are similar to the one obtained in the samples by arc melting. However, the difference in the preparation method led to a very different pinning landscape. While the behavior of arc-melted samples is described by the surface pinning model, the SPS sintered sample includes also point pinning defects that sum up to the contribution of the surface pinning. This leads to a J_c of 30.5 kA/cm² at 2 K and 0.01 T and 73.2 kA/cm² at 4 K and 0.01 T, values that are 286% and 687% larger, respectively, to those obtained in the arc-melted sample [21]. Samples with exactly the same composition were also prepared by hot-press sintering. Also these samples show a similar T_c = 7.9 K as samples prepared by arc melting [22].

However, the most remarkable and interesting advances in alternative preparation methods are observed in the HEA films. The first work about HEA films was published by Zhang et al. and was about the preparation of $(TaNb)_{100-x}(HfZrTi)_x$ films on Si substrates by DC magnetron co-sputtering at room temperature [24]. These films, with different stoichiometries and thicknesses (between 600 and 950 nm), crystallize, like their bulk relative, into a bcc structure. All the films are superconducting with T_c values in the range of 2.77–6.76 K. The largest T_c is found for a x = 43, and it is around 1 K lower than the bulk sample with the same composition due to, probably, the confined-size effect. The largest $B_{c2}(0)$ = 11.05 T is found, however, for x = 65, which even exceeds the Pauli paramagnetic limit [24]. Films of a different stoichiometry of the same system, the $(TaNb)_{70}(HfZrTi)_{30}$, were also deposited by magnetron sputtering to investigate how the thickness and the external hydrostatic pressure affect the superconducting properties. It was proved that both T_c and $B_{c2}(0)$ decay with decreasing thickness. The T_c values decrease from the original 7.8 K for the bulk to 5.31 K for the 600 nm film and 2.69 K for the 100 nm film. Films with a thickness of 30 nm are not superconducting. The same trend is observed for $B_{c2}(0)$, with values of 6.7, 5.8, and 3.2 T, for bulk, 600 nm and 100 nm, respectively. The application of hydrostatic pressure up to 3.3 GPa has different consequences depending on the thickness of the film. In the case of the 600 nm film, T_c decreases with the pressure, which is different from the behavior observed on the bulk samples. However, no significant T_c change was observed when pressure was applied to the 100 nm film. This could indicate, as expected, that thinner films increase the disorder due to amorphization [25]. The same deposition technique was used in the work of Shu et al. to deposit $(TaNbZrTi)_{100-x}W_x$ and $(TaNbZrTi)_{100-x}V_x$ superconducting films. In this work, the influence of alloying the TaNbZrTi-based system with W and V and the deposition temperature on the phase formation and superconducting behavior of the films was investigated. The results show that all the films with different values of x show a bcc structure similar to the original TaNbZrTi system. In terms of T_c values, the highest one, 8.0 K, was reached for the original TaNbZrTi system. Then, for both alloying elements, T_c dropped monotonically as a function of x, almost at the same rate. When increasing the deposition temperature from room temperature to 400°C, T_c increases while the compositions remain unchanged. Moreover, the experimental observations led to the conclusion that the T_c values may also relate to the atomic radii difference and electronegativity difference of involved elements beyond the valence electron number [26]. A very similar study was done by Zhang et al. with $(TaNb)_{100-x}(HfZrTi)_xMo_y$ films. Films with different stoichiometries of ~300 nm were deposited on Si substrates by magnetron sputtering. The films show again a bcc structure for low x values. For near-equimolar

composition, the crystalline HEA grains transform into amorphous aggregations with a size of a few nanometers, forming a crystal/glass nanocomposite. This particular microstructure causes a broadening of the normal-to-superconducting transition and suppresses the zero-resistivity critical temperature to a lower constant value of approximately 2.9 K [40]. A different technique, namely pulsed laser deposition (PLD), was employed by Jung et al. to deposit $Ta_{1/6}Nb_{2/6}Hf_{1/6}Zr_{1/6}Ti_{1/6}$ films. This HEA, studied in several works in bulk samples, was deposited on Al_2O_3 substrates at different temperatures ranging from 270 to 620°C. These films, which crystallize as expected in bcc structure, show T_c values between ~5.4 and 7.3 K, being the maximum value for deposition temperature of 520°C. Also, for the same deposition temperature, the largest $B_{c2}(0)$ = 12.1 T is observed. All films showed significantly larger J_c values than the bulk sample, while a self-field value above 1 MA/cm^2 (~ 1.8 MA/cm^2) at 4.2 K was measured for the film deposited at 520°C. The J_c values were maintained above 0.1 MA/cm^2 under magnetic fields of approximately 3.4 and 2.0 T at 2.0 and 4.2 K, respectively, which is approximately eight times larger than in the bulk sample at the same conditions. Another remarkable result of this work is the effect of ion irradiation on the properties of the films. It was demonstrated that the HEA films are over 1000 times more robust to ion irradiation than other superconducting materials, such as Nb_3Sn, MgB_2, Fe-based superconductors, or *RE*BCO. This means that the T_c of this HEA remains stable for much larger ion doses [23].

2.4 Other alloys

Rather different from the Ta-Nb-Hf-Zr-Ti system are the pentanary $(ScZrNb)_{1-x}[RhPd]_x$ and hexanary $(ScZrNbTa)_{100-x}[RhPd]_x$ systems reported by Stolze et al. [41]. They have investigated several mixtures of five and six elements showing a CsCl-type lattice, which is an ordered bcc structure, but had not been found in the original Ta-Nb-Hf-Zr-Ti system. It was also observed that T_c increases gradually with decreasing valence electron count (VEC) within a solution series. The highest T_c and $B_{c2}(0)$ are observed in the particular case of $(ScZrNb)_{65}[RhPd]_{35}$ with values of ~9.3 K and 10.7 T, respectively. Another important parameter that was observed in this case was the chemical composition, where the presence of niobium has a positive impact on the superconductivity. In any case, also samples without any niobium were superconducting proving that superconductivity is an intrinsic feature of the bulk material and not just an average of the constituents' elemental properties [26]. The elastic properties of such a hexanary HEA superconductor, $(ScZrNbTa)_{68.5}[RhPd]_{31.5}$, was investigated by Pan et al. [42]. Its Young's modulus E = 121.0 GPa and shear modulus of G = 44.9 GPa are around 10% larger than for Nb-Ti of similar T_c and ductility, which is promising for applications.

The authors of Ref. [41] reported also on three other new pentanary systems: $(ZrNb)_{1-x}[MoReRu]_x$, $(HfTaWIr)_{100-x}[Re]_x$, and $(HfTaWPt)_{100-x}[Re]_x$, which crystallize in a bcc α-Mn-type structure firstly observed in superconducting HEAs here [43]. The last two systems reported in this work are the first purely 5d-metal-based superconducting HEAs. Several stoichiometries were tested, showing T_c values between 2.1 K and 6.3 K. Just as in the case of type A Re-Nb-Hf-Zr-Ti, the presence of Re is important to understand the behavior of these systems. Here, Re plays a key role in the stabilization of this structure type [23]. Liu et al. [44] observed the same α-Mn-type structure in $Nb_{25}Mo_{5+x}Re_{35}Ru_{25-x}Rh_{10}$ ($0 \leq x \leq 10$), of which $Nb_{25}Mo_{10}Re_{35}Ru_{20}Rh_{10}$ shows the largest T_c = 5.1 K and $B_{c2}(0)$ = 8.3 T [41].

The general tendency of the superconducting HEAs to crystallize in cubic structures was not followed by the discovery of the $Re_{56}Nb_{11}Ti_{11}Zr_{11}Hf_{11}$ alloy by Marik et al. [45], the first hexagonal superconducting HEA. These HEAs with hexagonal-close-packed (hcp) structure are in general rather interesting from the practical point of view because of their high hardness. $Re_{56}Nb_{11}Ti_{11}Zr_{11}Hf_{11}$ has a T_c = 4.4 K, $B_{c1}(0)$ = 2.3 mT, and $B_{c2}(0)$ = 3.6 T [42]. Other superconducting HEAs crystallizing in hcp structure are, for example, $(MoReRuRh)_{95}Ti_5$ and $(MoReRuRh)_{90}Ti_{10}$ with T_c = 3.6 K and 4.7 K, respectively [46], or $Nb_{10+2x}Mo_{35-x}Ru_{35-x}Rh_{10}Pd_{10}$ ($0 \leq x \leq 5$) with a maximum T_c = 6.19 K for x = 2.5 [47]. A variant of the archetypical hcp structure is found in transition-metal antimonides $M_{1-x}Pt_xSb$ (M = equimolar mix of Ru, Rh, Pd, and Ir) that crystallize in a pseudo-hexagonal NiAs-type crystal structure [48]. The synthesis for various Pt contents, x, and heat treatment conditions lead to entropy-stabilized transition-metal monoantimonides. Superconductivity was only found for a particular composition, x = 0.2, for which a superconducting transition at T_c = 2.15 was observed. This T_c is similar to the highest values previously reported for transition-metal monoantimonides [45].

A transformation from the original hcp structure to a new face-centered cubic (fcc) one was observed in $(MoReRu)_{(1-2x)/3}(PdPt)_x$ and carbon-added $(MoReRu)_{(1-2x)/3}(PdPt)_xC_y$ HEAs by Zhu et al. [49]. The $(MoReRu)_{(1-2x)/3}(PdPt)_x$ alloys were found to crystallize in an hcp structure for $0.042 \leq x \leq 0.167$ and in an fcc structure for x = 0.333. Their VEC values are somewhat outside the expected ranges, between 7.0 and 8.0. The addition of a certain amount of C that depends on x causes also a transformation to the fcc structure. As in the C-free case, the structural transformation is likely driven by the combined effects of VEC, lattice distortion, and increase in entropy. The T_c values of the hcp phases range from 1.75 K to 8.17 K, while the ones of the fcc structures are always below 2.8 K [46].

A different crystal structure is observed in the $Ta_5[Mo_{35-x}W_{5+x}]Re_{35}Ru_{20}$ and $[Ta_{5+y}Mo_{35-y}]W_5Re_{35}Ru_{20}$ HEAs [8]. In this case, the HEAs crystallize into tetragonal sigma (σ) phases. These systems exhibit fully gapped bulk superconductivity with T_c values between 5.27 K and 6.29 K, reaching the maximum at $x = y = 0$ [47]. The same type of structure was observed in $Ta_{10}Mo_{35-x}Cr_xRe_{35}Ru_{20}$ ($5 \leq x \leq 13$) [50], highlighted by the presence of Cr, which is not commonly found in superconducting materials. These HEAs exhibit T_c values up to 4.79 K and show a paramagnetic behavior in the normal state due to the magnetic moment of Cr [48].

A transformation from the σ-phase into a new structure happens in $Ta_{10}Mo_5W_{30}Re_{35}Ru_{20}$ upon adding C [51]. The $Ta_{10}Mo_5W_{30}Re_{35}Ru_{20}C_x$ HEA crystallizes in the centrosymmetric σ-type structure for $0 \leq x \leq 2$ but transforms into the noncentrosymmetric β-Mn structure for $16 \leq x \leq 20$. The HEA with the β-Mn structure shows T_c = 5.34 K, which is larger than for the original σ-type structure. The $B_{c2}(0)$ = 9.3 T is close to the Pauli paramagnetic limit. This phase transformation is likely caused by the decrease in VEC and the increase in lattice distortion and mixing entropy [49]. The same β-Mn structure is found in the $Cr_{5+x}Mo_{35-x}W_{12}Re_{35}Ru_{13}C_{20}$ HEA $0 \leq x \leq 9$ [52]. By increasing x, T_c was observed to decrease from 5.49 K to 3.35 K due to the magnetic pair breaking caused by Cr moments. For all the different stoichiometries, $B_{c2}(0)$ is comparable to the Pauli paramagnetic limit $B_P(0) = 1.86T_c$, having a maximum value of 9.7 T [50].

Based on the relationship between the VEC and T_c values for HEAs and other binary or ternary superconducting alloys, new combinations of elements and stoichiometries were tested approaching the VEC values where superconductivity appears. As a result, several new HEA systems have been discovered. One example is the new

boron-based HEA superconductor $Mo_{11}W_{11}V_{11}Re_{34}B_{33}$ (MWVRB) [53]. With a VEC = 5.24, this compound crystallized in the tetragonal $CuAl_2$ crystal structure and showed a T_c = 4.0 K and a $B_{c2}(0)$ = 7.3 T [51]. For a summary of these HEAs different from TaNbHfZrTi basis, see **Table 4**.

Structure	Nominal composition	T_c (K)	$B_{c2}(0)$ (T)	Reference
CsCl	$(ScZrNb)_{60}[RhPd]_{40}$	5.20	2.10	[41]
	$(ScZrNb)_{62}[RhPd]_{38}$	9.20	8.90	[41]
	$(ScZrNb)_{63}[RhPd]_{37}$	9.30	9.60	[41]
	$(ScZrNb)_{65}[RhPd]_{35}$	9.70	10.70	[41]
	$(ScZrNbTa)_{67}[RhPd]_{33}$	4.20	2.10	[41]
	$(ScZrNbTa)_{684}[RhPd]_{316}$	6.40	8.80	[41]
	$(ScZrNbTa)_{685}[RhPd]_{315}$	7.0		[42]
α-Mn	$(ZrNb)_{10}[MoReRu]_{90}$	5.30	7.86	[43]
	$(HfTaWIr)_{20}[Re]_{80}$	5.90	—	[43]
	$(HfTaWIr)_{40}[Re]_{60}$	4.00	4.64	[43]
	$(HfTaWPt)_{20}[Re]_{80}$	6.30	—	[43]
	$(HfTaWPt)_{40}[Re]_{60}$	4.40	5.90	[43]
	$(HfTaWPt)_{50}[Re]_{50}$	2.40	—	[43]
	$Nb_{25}Mo_5Re_{35}Ru_{25}Rh_{10}$	4.66	7.50	[44]
	$Nb_{25}Mo_{10}Re_{35}Ru_{20}Rh_{10}$	5.10	8.30	[44]
	$Nb_{25}Mo_{15}Re_{35}Ru_{15}Rh_{10}$	5.10	7.90	[44]
	$Nb_5Mo_{35}Re_{15}Ru_{35}Rh_{10}$	7.54	8.90	[44]
	$Nb_5Mo_{30}Re_{20}Ru_{35}Rh_{10}$	6.69	7.50	[44]
	$Nb_5Mo_{25}Re_{25}Ru_{35}Rh_{10}$	6.51	7.50	[44]
	$Nb_5Mo_{20}Re_{30}Ru_{35}Rh_{10}$	5.46	6.10	[44]
hcp	$Re_{56}Nb_{11}Ti_{11}Zr_{11}Hf_{11}$	4.40	3.60	[45]
	$(MoReRuRh)_{95}Ti_5$	3.60	—	[46]
	$(MoReRuRh)_{90}Ti_{10}$	4.70	—	[46]
	$Nb_{10}Mo_{35}Ru_{35}Rh_{10}Pd_{10}$	5.58	6.90	[47]
	$Nb_{15}Mo_{32.5}Ru_{32.5}Rh_{10}Pd_{10}$	6.19	8.10	[47]
	$Nb_{20}Mo_{30}Ru_{30}Rh_{10}Pd_{10}$	6.10	8.30	[47]
	$Mo_{30}Re_{29}Ru_{36}Pd_1Pt_4$	8.17	—	[49]
	$Mo_{27}Re_{25}Ru_{34}Pd_5Pt_9$	4.91	—	[49]
	$Mo_{24}Re_{20}Ru_{30}Pd_{12}Pt_{14}$	2.22	—	[49]
	$Mo_{22}Re_{22}Ru_{28}Pd_{10}Pt_{18}$	1.64	—	[49]
NiAs	$(RuRhPdIr)_{80}Pt_{20}Sb$ (SSR)	2.15	—	[48]
fcc	$Mo_{28}Re_{28}Ru_{35}Pd_4Pt_5C_{30}$	2.46	—	[49]
	$Mo_{29}Re_{27}Ru_{36}Pd_4Pt_4C_{44}$	2.72	—	[49]
	$Mo_{26}Re_{25}Ru_{33}Pd_8Pt_9C_{27}$	2.28	—	[49]

Structure	Nominal composition	T_c (K)	$B_{c2}(0)$ (T)	Reference
	$Mo_{27}Re_{25}Ru_{34}Pd_6Pt_9C_{40}$	2.30	—	[49]
	$Mo_{26}Re_{22}Ru_{31}Pd_9Pt_{13}C_{22}$	1.86	—	[49]
	$Mo_{23}Re_{23}Ru_{30}Pd_{11}Pt_{14}C_{31}$	1.91	—	[49]
	$Mo_{21}Re_{21}Ru_{27}Pd_{13}Pt_{18}C_{25}$	1.87	—	[49]
	$Mo_{21}Re_{22}Ru_{27}Pd_{14}Pt_{17}C_{30}$	1.75	—	[49]
σ-type	$Ta_5Mo_{35}W_5Re_{35}Ru_{20}$	6.29	—	[8]
	$Ta_5Mo_{30}W_{10}Re_{35}Ru_{20}$	6.20	—	[8]
	$Ta_5Mo_{25}W_{15}Re_{35}Ru_{20}$	6.10	—	[8]
	$Ta_5Mo_{20}W_{20}Re_{35}Ru_{20}$	5.69	—	[8]
	$Ta_5Mo_{15}W_{25}Re_{35}Ru_{20}$	5.46	—	[8]
	$Ta_5Mo_{10}W_{30}Re_{35}Ru_{20}$	5.45	—	[8]
	$Ta_5Mo_5W_{35}Re_{35}Ru_{20}$	4.78	—	[8]
	$Ta_7Mo_{33}W_5Re_{35}Ru_{20}$	6.13	—	[8]
	$Ta_9Mo_{31}W_5Re_{35}Ru_{20}$	5.70	—	[8]
	$Ta_{11}Mo_{29}W_5Re_{35}Ru_{20}$	5.32	—	[8]
	$Ta_{13}Mo_{27}W_5Re_{35}Ru_{20}$	5.27	—	[8]
	$Ta_{10}Mo_{30}Cr_5Re_{35}Ru_{20}$	4.79	6.10	[50]
	$Ta_{10}Mo_{25}Cr_{10}Re_{35}Ru_{20}$	4.41	5.80	[50]
	$Ta_{10}Mo_{22}Cr_{13}Re_{35}Ru_{20}$	3.98	4.90	[50]
	$Ta_{10}Mo_5W_{30}Re_{35}Ru_{20}$	4.87	6.70	[51]
	$Ta_{10}Mo_5W_{30}Re_{35}Ru_{20}C_2$	4.80	—	[51]
β-Mn	$Ta_{10}Mo_5W_{30}Re_{35}Ru_{20}C_{16}$	5.36	—	[51]
	$Ta_{10}Mo_5W_{30}Re_{35}Ru_{20}C_{18}$	5.32	—	[51]
	$Ta_{10}Mo_5W_{30}Re_{35}Ru_{20}C_{20}$	5.34	9.30	[51]
	$Cr_5Mo_{35}W_{12}Re_{35}Ru_{13}C_{20}$	5.49	9.70	[52]
	$Cr_8Mo_{32}W_{12}Re_{35}Ru_{13}C_{20}$	4.73	8.40	[52]
	$Cr_{11}Mo_{29}W_{12}Re_{35}Ru_{13}C_{20}$	3.83	7.30	[52]
	$Cr_{14}Mo_{26}W_{12}Re_{35}Ru_{13}C_{20}$	3.35	5.30	[52]
$CuAl_2$	$Mo_{11}W_{11}V_{11}Re_{34}B_{33}$	4.00	7.30	[53]

Table 4.
Selected properties of non-bcc structure-type HEA superconductors. SSR solid-state reaction; all other samples prepared by arc melting.

3. Superconducting high-entropy compounds

3.1 Intermetallics

Other high-entropy superconductors with different compositions present alternative structures to the previous ones, **Table 5**. For example, $(V_{0.5}Nb_{0.5})_{3-x}Mo_xAl_{0.5}Ga_{0.5}$ ($0.2 < x \leq 1.4$) is polymorphic with bcc and A15 structure (similar to α- and β-W

Structure	Nominal composition	T_c (K)	$B_{c2}(0)$ (T)	Reference
A15	$(V_{0.5}Nb_{0.5})_{2.8}Mo_{0.2}Al_{0.5}Ga_{0.5}$	10.20	20.10	[7]
	$(V_{0.5}Nb_{0.5})_{2.6}Mo_{0.4}Al_{0.5}Ga_{0.5}$	9.20	17.70	[7]
	$(V_{0.5}Nb_{0.5})_{2.4}Mo_{0.6}Al_{0.5}Ga_{0.5}$	8.90	17.00	[7]
	$(V_{0.5}Nb_{0.5})_{2}Mo_{1}Al_{0.5}Ga_{0.5}$	6.10	9.90	[7]
	$(V_{0.5}Nb_{0.5})_{1.8}Mo_{1.2}Al_{0.5}Ga_{0.5}$	4.80	7.60	[7]
	$(V_{0.5}Nb_{0.5})_{1.6}Mo_{1.4}Al_{0.5}Ga_{0.5}$	3.20	4.80	[7]
	$V_5Nb_{35}Mo_{35}Ir_{10}Pt_{15}$	5.18	6.40	[55]
	$V_{15}Nb_{30}Mo_{30}Ir_{10}Pt_{15}$	4.49	5.70	[55]
	$V_{25}Nb_{25}Mo_{25}Ir_{10}Pt_{15}$	3.61	4.40	[55]
	$Nb_3Al_{0.2}Sn_{0.2}Ge_{0.2}Ga_{0.2}Si_{0.2}$	9.00	10.40	[56]
	$Nb_3Al_{0.3}Sn_{0.3}Ge_{0.2}Ga_{0.1}Si_{0.1}$	11.00	13.30	[56]
	$V_3Al_{0.07}Si_{0.30}Ga_{0.08}Ge_{0.30}Sn_{0.25}$	6.30	8.8	[57]
CuAl$_2$	$Co_{0.2}Ni_{0.1}Cu_{0.1}Rh_{0.3}Ir_{0.3}Zr_2$	8.0	12	[58]
	$Fe_{0.09}Co_{0.19}Ni_{0.11}Rh_{0.27}Ir_{0.33}Zr_2$	7.8	8.5	[54]
	$Fe_{0.11}Co_{0.30}Ni_{0.20}Rh_{0.07}Ir_{0.32}Zr_2$	6.7	6.6	[54]
	$Fe_{0.19}Co_{0.19}Ni_{0.20}Rh_{0.21}Ir_{0.21}Zr_2$	5.4	5.5	[54]
	$Fe_{0.29}Co_{0.19}Ni_{0.30}Rh_{0.09}Ir_{0.12}Zr_2$	4.8	4.8	[54]
	$Fe_{0.09}Co_{0.20}Ni_{0.20}Cu_{0.17}Rh_{0.19}Ir_{0.15}Zr_2$	5.7		[59]

Table 5.
Selected properties of A15 and TrZr$_2$ high-entropy superconductors. All samples have been prepared by arc melting. The compositions of Ref. [54] were rounded to two decimals for simplicity.

actually) [7]. Furthermore, heating also induces a polymorphic transformation from original bcc structure to the A15 one, as shown for $x = 0.2$. The resulting compound with this A15 structure shows bulk superconductivity with $T_c = 10.2$ K and an estimated $B_{c2}(0) = 20.1$ T [52]. Here, mixing on both distinct lattice sites occurs, and a true alloy resembling β-W is forming. A similar case is the system $V_{5+2x}Nb_{35-x}Mo_{35-x}Ir_{10}Pt_{15}$ ($0 \leq x \leq 10$) with maximum $T_c = 5.18$ K and $B_{c2}(0) = 6.4$ T for $x = 0$ [55].

The A15 structure type can be also found in high-entropy compounds like $Nb_3Al_{0.2}Sn_{0.2}Ge_{0.2}Ga_{0.2}Si_{0.2}$ with a $T_c = 9.0$ K and $B_{c2}(0) = 10.4$ T [56], $Nb_3Al_{0.3}Sn_{0.3}Ge_{0.2}Ga_{0.1}Si_{0.1}$ with a $T_c = 11.0$ K and $B_{c2}(0) = 13.3$ T [56], and $V_3Al_{0.07}Si_{0.30}Ga_{0.08}Ge_{0.30}Sn_{0.25}$ with a $T_c = 6.3$ K and $B_{c2}(0) = 8.8$ T [57]. In all these cases, mixing occurs primarily on just one of the lattice sites (disregarding natural disorder), and a compound resembling Cr_3Si (or Nb_3Sn, for that matter) is formed. The V system is also interesting because it introduced the concept of compositionally complex alloys (CCAs) as a new category of multi-principal-element materials closely related to high-entropy alloys, but containing more than two phases in an alloy sample. In the particular case of $V_3Al_{0.07}Si_{0.30}Ga_{0.08}Ge_{0.30}Sn_{0.25}$, it crystallizes into five high-entropy A15 phases with different compositions. This concept of CCAs is thought to be a practical way to improve the properties of the superconducting HEAs.

Further high-entropy intermetallics are the so-called $TrZr_2$ compounds (Tr (mix of) transition metal) with $CuAl_2$ crystal structure. They have been discovered by

Mizuguchi et al. in $Co_{0.2}Ni_{0.1}Cu_{0.1}Rh_{0.3}Ir_{0.3}Zr_2$ and can be regarded as mixing of single-*Tr* zirconides, of which many are superconductors themselves [58]. This high-entropy compound shows a T_c of 8.0 K and a $B_{c2}(0)$ of 12 T. Shortly after, superconductivity was also found in $(Fe,Co,Ni,Rh,Ir)Zr_2$ samples of different stoichiometries [54]. The same group found an unusual broadening of the specific heat jump at T_c for this system (developing with the number of *Tr* elements), which they attributed to an inhomogeneity of the Cooper pair formation and hence the superconducting gap [59]. Pugliese et al. [60] investigated possible local inhomogeneities in these systems by extended X-ray absorption fine structure (EXAFS) measurements and found a correlation between T_c and the Zr $4d$-*Tr* nd hybridization. The Zr-Zr bonds seem to get stiffer with increasing mixing entropy, which suggests nanoscale texturing with possible local order.

3.2 Non-oxide ceramics

The concept of high-entropy alloys primarily focused on metal alloys, however, was quickly extended to other types of materials, **Table 6**. This approach, centered on maximizing the configurational entropy to stabilize equimolar or near-equimolar mixtures, was employed in a mixture of oxides to synthesize the first high-entropy oxide (HEO) in 2015 [71], giving rise to a new category known as high-entropy ceramics (HECs). HECs encompass all high-entropy materials with ceramic properties. Similar to HEAs, HECs consist of multicomponent elements in a single phase,

Structure	Nominal composition	T_c (K)	$B_{c2}(0)$ (T)	Reference
NaCl	$(TiZrNbHfTa)C$	2.35	0.51	[62]
	$(MoNbTaVW)C_{0.9}$	3.4	3.37	[63]
	$(AgInSnPbBi)Te$	2.6	2.8	[64]
	$(\{AgSnPbBi\}_{(1-x)/4}In_x)Te$	<2.8	—	[65]
1 T-NiTe$_2$	$(Co,Au)_{0.2}(Rh,Ir,Pd,Pt)_{0.8}Te_2$	4.5	—	[66]
	$Co_{0.03}Au_{0.06}Rh_{0.23}Ir_{0.24}Pd_{0.16}Pt_{0.28}Te_2$	2.5	—	[66]
W$_5$Si$_3$	$(Nb_{0.1}Mo_{0.3}W_{0.3}Re_{0.2}Ru_{0.1})_5Si_3$	3.30	5.00	[67]
	$(Nb_{0.2}Mo_{0.3}W_{0.3}Re_{0.1}Ru_{0.1})_5Si_3$	3.20	5.10	[67]
LaOBiS2	$La_{0.1}Ce_{0.1}Pr_{0.2}Nd_{0.3}Sm_{0.3}O_{0.5}F_{0.5}BiS_2$	4.9		[68]
	$La_{0.2}Ce_{0.2}Pr_{0.2}Nd_{0.2}Sm_{0.2}O_{0.5}F_{0.5}BiS_2$	3.97		[69]
	$La_{0.3}Ce_{0.3}Pr_{0.2}Nd_{0.1}Sm_{0.1}OBiS_2$	3.4	0.65/11	[61]
	$La_{0.1}Ce_{0.3}Pr_{0.3}Nd_{0.2}Sm_{0.1}OBiS_2$	4.3	0.69/15	[61]
	$La_{0.2}Ce_{0.2}Pr_{0.2}Nd_{0.2}Sm_{0.2}OBiS_2$	3.3	0.24/4.9	[61]
	$La_{0.1}Ce_{0.3}Pr_{0.1}Nd_{0.2}Sm_{0.3}OBiS_2$	4.6	0.42/16	[61]
	$La_{0.1}Ce_{0.3}Pr_{0.3}Nd_{0.1}Sm_{0.2}OBiS_2$	3.7		[70]
	$La_{0.2}Ce_{0.3}Pr_{0.3}Sm_{0.1}Gd_{0.1}OBiS_2$	3.0		[70]
	$La_{0.2}Ce_{0.3}Pr_{0.2}Nd_{0.1}Sm_{0.1}Gd_{0.1}OBiS_2$	2.9		[70]

Table 6.
Selected properties of high-entropy superconducting ceramics. For Ref. [61], $B_{c2}(0)$ is given for both major field directions, B∥c and B⊥c.

where their substantial configurational entropy plays a crucial role in their formation. In contrast to metallic HEAs, HECs typically exhibit semiconductor or insulator characteristics, making them potentially useful as functional materials. These systems have proven to be versatile in various technologies, including thermal barrier coatings, thermoelectrics, catalysts, and batteries, as well as wear-resistant and corrosion-resistant coatings [72–74]. However, in this chapter, the focus will be on those materials that show superconducting properties.

High-entropy carbide ceramics (HECCs) are a subgroup of materials belonging to the more general one of the HEC. The high-entropy carbides are coming from the binary transition metal carbides (*TMC*s), composed of carbon and a transition metal, that are widely used as ultra-high-temperature ceramics in structural applications. They are made by combining different *TMC*s to synthesize a single-phase multi-principal elemental HECC [75]. Among them, (TiZrNbHfTa)C was the first one to show superconducting properties [62]. This HECC, prepared by SPS, crystallizes in NaCl structure and shows bulk superconductivity with T_c = 2.35 K, $B_{c1}(0) \sim 26.1$ mT, and $B_{c2}(0) \sim 0.51$ T. Those superconducting properties are robust and were kept almost invariable under pressure up to 80 GPa [74]. Very recently, Shu et al. discovered the coexistence of ferromagnetism and superconductivity in (MoNbTaVW)C$_{0.9}$ and (TaTiNbZr)C [63].

Some superconducting telluride high-entropy compounds crystallize in the NaCl structure too (**Figure 2b**). Superconductivity was first seen in AgInSnPbBiTe$_5$ by Mizuguchi with a T_c of $\sim$2.6 K and an extrapolated $B_{c2}(0)$ of $\sim$2.8 T [64]. Upon applying pressure up to 35 GPa, the crystal structure changes via a Pnma structure (at around 12 GPa) to the CsCl type with increased T_c values of $\sim$5.3 K [76]. The stoichiometry on the *M* site was varied shortly after by adjusting the In content as (AgSnPbBi)$_{(1-x)/4}$In$_x$Te with x = 0, 0.1, 0.2, 0.3, and 0.4, where the sample without In is not superconducting, and T_c increases slightly with x [65]. A special case of superconducting high-entropy tellurides is (Co,Au)$_{0.2}$(Rh,Ir,Pd,Pt)$_{0.8}$Te$_2$ and Co$_{0.03}$Au$_{0.06}$Rh$_{0.23}$Ir$_{0.24}$Pd$_{0.16}$Pt$_{0.28}$Te$_2$ as layered compounds with 1 T-NiTe$_2$ structure. They are called high-entropy van der Waals materials (HEX) and show superconductivity up to 4.5 K [66].

The case of the high-entropy silicides (HESs) is quite similar to the carbides. They are made by combining Si with other elements, mainly metals. The binary transition-metal silicides M_5Si$_3$ were studied extensively for high-temperature structural applications due to their high melting points. Again, combining these binary silicides, different HESs were synthesized. However, the first superconducting high-entropy silicides appeared only very recently [67]. (Nb$_{0.1}$Mo$_{0.3}$W$_{0.3}$Re$_{0.2}$Ru$_{0.1}$)$_5$Si$_3$ and (Nb$_{0.2}$Mo$_{0.3}$W$_{0.3}$Re$_{0.1}$Ru$_{0.1}$)$_5$Si$_3$ were prepared by arc melting and are weakly coupled bulk superconductors. They both crystallize in the W$_5$Si$_3$ structure and have T_c values of 3.3 K and 3.2 K, and $B_{c2}(0)$ values of 5.0 T and 5.1 T, respectively [65].

Superconducting high-entropy sulfides are derived from the layered superconductors *RE*(O,F)BiS$_2$ by mixing the rare earth element (*RE*) (**Figure 2c**)[77]. The first reported system was (La,Pr,Ce,Nd,Sm)O$_{0.5}$F$_{0.5}$BiS$_2$, where T_c depends linearly on lattice parameter a, and La$_{0.1}$Ce$_{0.1}$Pr$_{0.2}$Nd$_{0.3}$Sm$_{0.3}$O$_{0.5}$F$_{0.5}$BiS$_2$ showed the highest value of $\sim$4.9 K [68]. The same group investigated shortly after the dependence of structural and superconducting properties on the mixing entropy by compounds with one to five *RE* elements, where T_c and superconducting volume fraction increase linearly with mixing entropy [69]. Shortly after, superconductivity was also confirmed in F-free *HE RE*OBiS$_2$ single crystals [61, 70], for which the anisotropy of the upper critical field could be determined.

3.3 Oxides

The first high-entropy oxides (HEOs) were reported by Rost et al. in 2015 [71]. In this work, the authors demonstrated that the entropy drives a reversible solid-state transformation between a multiphase and a single-phase state and was able to synthesize $(Mg_{0.2}Co_{0.2}Ni_{0.2}Cu_{0.2}Zn_{0.2})O$, the first HEO [61]. However, the term HEO was only introduced 1 year later by Bérardan et al., making the analogy to HEAs, to classify these multicationic, equiatomic oxide systems [78]. Over the years, the HEOs have gained significant interest due to their unique structural characteristics and related possibilities for tailoring functional properties [79–82]. One particularity of the HEOs, in contrast to HEAs, is that here the elemental mixing is restricted to one or only some of the atomic positions, similar to the metallic and ceramic compounds mentioned above. Superconductivity in HEOs could only be found in compounds of the $REBa_2Cu_3O_{7-\delta}$ (REBCO) family so far, probably the best-known and studied superconducting oxides. A recent search, for example, for superconducting high-entropy Ruddlesden-Popper cuprates has not been successful so far [83].

The concept of HEO was applied for the first time to REBCO compounds in 2020 by Shukunami et al. when the first high-entropy REBCO (HE REBCO) compound was reported [10]. The REBCO compounds exhibit a triple perovskite structure, whose center is the RE atom. This RE site is occupied with a mixture of rare earth elements, so that is where entropy is introduced (**Figure 2d**).

To the best of our knowledge, although the number has been increasing year by year since 2020, only 10 articles have been reported on HE REBCO to date. The different HE REBCO compounds presented in those articles can be classified as bulks or films according to the synthesis method followed (**Table 7**). Within the group of the films, one can further distinguish between films by pulsed laser deposition (PLD) and by chemical solution deposition (CSD).

Shukunami et al. manufactured polycrystalline REBCO bulk samples via solid-state reaction, combining up to six different rare earths in 2020 [10]. So far, all bulk HE REBCO samples have been prepared by SSR. In particular, they presented $Y_{0.28}Nd_{0.16}Sm_{0.18}Eu_{0.18}Gd_{0.20}Ba_2Cu_3O_{7-\delta}$ and $Y_{0.18}La_{0.24}Nd_{0.14}Sm_{0.14}Eu_{0.15}Gd_{0.15}Ba_2Cu_3O_{7-\delta}$ as the first two superconducting HE REBCO compounds with T_c = 93 K in both cases. The J_c values of these compounds were calculated from magnetic measurements at 2 K and 1 T. The values were 11.7 kA/cm^2 for $Y_{0.28}Nd_{0.16}Sm_{0.18}Eu_{0.18}Gd_{0.20}Ba_2Cu_3O_{7-\delta}$ (~20 kA/cm^2 at self-field) and 8.1 kA/cm^2 for $Y_{0.18}La_{0.24}Nd_{0.14}Sm_{0.14}Eu_{0.15}Gd_{0.15}Ba_2Cu_3O_{7-\delta}$. The authors also identify a clear correlation between T_c and the orthorhombicity parameter (OP), which is defined as $2|a - b|/(a+b)$ with lattice constants a and b. For $OP > 0.012$, the T_c of the samples is almost constant, but for $OP < 0.012$, T_c starts to decay. For $OP < 0.007$, superconductivity was not observed anymore. Interestingly and accordingly, two further HE REBCO compounds that they prepared were not superconducting, namely, $Y_{0.23}La_{0.25}Nd_{0.15}Sm_{0.19}Eu_{0.18}Ba_2Cu_3O_{7-\delta}$ and the $Y_{0.23}La_{0.23}Nd_{0.17}Sm_{0.18}Gd_{0.19}Ba_2Cu_3O_{7-\delta}$. These results indicate the importance of wisely selecting the RE elements to include in the HE REBCO to maximize the superconducting properties. One year later, Wang et al. [84] prepared four new HE REBCO compounds with a mixture of five elements in each case: $Y_{0.2}La_{0.2}Sm_{0.2}Dy_{0.2}Er_{0.2}Ba_2Cu_3O_{7-\delta}$, $Y_{0.2}Ho_{0.2}Er_{0.2}Tm_{0.2}Yb_{0.2}Ba_2Cu_3O_{7-\delta}$, $Y_{0.5}La_{0.125}Sm_{0.125}Dy_{0.125}Er_{0.125}Ba_2Cu_3O_{7-\delta}$, and $Y_{0.5}Sm_{0.125}Eu_{0.125}Gd_{0.125}Dy_{0.125}Ba_2Cu_3O_{7-\delta}$. Magnetic measurements showed that all these samples exhibit a very similar T_c of ~92 K. The self-field J_c values of

Nominal composition on *RE* site	T_c (K)	J_c (MA/cm^2)	Reference
$Y_{0.28}Nd_{0.16}Sm_{0.18}Eu_{0.18}Gd_{0.20}$	93.0	0.02 (2 K, sf) 0.0117 (2 K, 1 T)	[10]
$Y_{0.18}La_{0.24}Nd_{0.14}Sm_{0.14}Eu_{0.15}Gd_{0.15}$	93.0	0.081 (2 K, 1 T)	[10]
$Y_{0.2}La_{0.2}Sm_{0.2}Dy_{0.2}Er_{0.2}$	92.0	—	[84]
$Y_{0.2}Ho_{0.2}Er_{0.2}Tm_{0.2}Yb_{0.2}$	92.0	—	[84]
$Y_{0.5}La_{0.125}Sm_{0.125}Dy_{0.125}Er_{0.125}$	92.0	0.02 (2 K, sf) 0.002 (77 K, sf)	[84]
$Y_{0.5}Sm_{0.125}Eu_{0.125}Gd_{0.125}Dy_{0.125}$	92.0	—	[84]
$Y_{0.2}La_{0.2}Sm_{0.2}Eu_{0.2}Gd_{0.2}$	93.4	0.0109 (JcGlobal at 2 K, 1 T) 6.5 (Jclocal at 2 K, sf)	[85]
$Y_{0.2}Nd_{0.2}Sm_{0.2}Eu_{0.2}Gd_{0.2}$	93.4	0.0117 (2 K, 1 T)	[85]
$Y_{0.2}Sm_{0.2}Eu_{0.2}Dy_{0.2}Ho_{0.2}$	93.0	0.0346 (2 K, 1 T)	[85]
$Y_{1/6}La_{1/6}Nd_{1/6}Sm_{1/6}Eu_{1/6}Gd_{1/6}$	93.1	0.0081 (2 K, 1 T)	[85]
$Y_{1/6}Sm_{1/6}Eu_{1/6}Dy_{1/6}Ho_{1/6}Yb_{1/6}$	92.0	0.0499 (2 K, 1 T)	[85]
$Y_{1/7}Sm_{1/7}Eu_{1/7}Dy_{1/7}Ho_{1/7}Yb_{1/7}Lu_{1/7}$	91.4	0.0535 (JcGlobal at 2 K, 1 T) 5.5 (Jclocal at 2 K, sf)	[85]
$Dy_{0.16}Ho_{0.17}Er_{0.20}Tm_{0.22}Yb_{0.25}$	88.8	—	[86]
$Gd_{0.23}Dy_{0.17}Ho_{0.15}Er_{0.15}Tm_{0.19}Yb_{0.20}$	89.8	—	[86]
$Gd_{0.20}Dy_{0.13}Ho_{0.10}Er_{0.15}Tm_{0.09}Yb_{0.20}Lu_{0.15}$	89.4	—	[86]
$Y_{0.12}Sm_{0.08}Eu_{0.26}Dy_{0.18}Ho_{0.36}$ (PLD film)	90.5	6.5 (2 K, 1 T) 2.3 (4.2 K, 7 T)	[87]
$Y_{0.7}Gd_{0.2}Dy_{0.2}Sm_{0.2}Eu_{0.2}$ (CSD film)	93.0	10 (30 K, sf) 4 (65 K, sf) 2 (77 K, sf)	[88]
$Gd_{0.2}Sm_{0.2}Nd_{0.2}Eu_{0.2}Y_{0.2}$ (CSD film)	90.4	2.4 (77 K, sf)	[89]
$Gd_{0.2}Dy_{0.2}Y_{0.2}Ho_{0.2}Er_{0.2}$ (+12% BHO, CSD)	91.9	3.5 (77 K, sf)	[90]

Table 7.
Critical temperatures and selected J$_c$ *data of high-entropy* RE*BCO phases. The samples, except otherwise stated, are prepared by solid-state reaction. sf, self-field or remanent state.*

$Y_{0.5}La_{0.125}Sm_{0.125}Dy_{0.125}Er_{0.125}Ba_2Cu_3O_{7-\delta}$ were 20 kA/cm^2 at 1.8 K and 2 kA/cm^2 at 77 K. These samples show smaller irreversible fields than traditional YBCO, indicating again that the selection of the *RE* elements has a huge influence on the properties of these compounds. In 2022, Yamashita et al. of the same group that reported the first HE *RE*BCO went a step further [85]. They prepared six new

compounds by solid-state reaction including one with seven different *RE*: $Y_{0.2}La_{0.2}Sm_{0.2}Eu_{0.2}Gd_{0.2}Ba_2Cu_3O_{7-\delta}$, $Y_{0.2}Nd_{0.2}Sm_{0.2}Eu_{0.2}Gd_{0.2}Ba_2Cu_3O_{7-\delta}$, $Y_{0.2}Sm_{0.2}Eu_{0.2}Dy_{0.2}Ho_{0.2}Ba_2Cu_3O_{7-\delta}$, $Y_{1/6}La_{1/6}Nd_{1/6}Sm_{1/6}Eu_{1/6}Gd_{1/6}Ba_2Cu_3O_{7-\delta}$, $Y_{1/6}Sm_{1/6}Eu_{1/6}Dy_{1/6}Ho_{1/6}Yb_{1/6}Ba_2Cu_3O_{7-\delta}$, and $Y_{1/7}Sm_{1/7}Eu_{1/7}Dy_{1/7}Ho_{1/7}Yb_{1/7}Lu_{1/7}Ba_2Cu_3O_{7-\delta}$. T_c values of these compounds are between 93.4 K and 91.4 K, slightly decreasing with *RE* complexity. Similar to their first work on T_c, they correlated the *OP* here with J_c. Again, there is an obvious correlation between both parameters, being the largest J_c = 53.5 kA/cm^2 (2 K, 1 T), for the largest *OP* that corresponds to the compound with seven *RE*, even though T_c was the smallest. This value of J_c, measured magnetically on cube-shaped samples, corresponds to J_c^{Global}. However, this J_c is affected by the typical weak links from grain to grain found in the *RE*BCO compounds due to their short coherence lengths. Therefore, the authors estimate J_c within the grains (J_c^{local}) in fine powders of the same composition as the samples by magnetic measurements. At 2 K, J_c^{local} of $\sim$6.5 MA/cm^2 was found for $Y_{0.2}Sm_{0.2}Eu_{0.2}Dy_{0.2}Ho_{0.2}Ba_2Cu_3O_{7-\delta}$ and $\sim$ 5.5 MA/cm^2 for $Y_{1/7}Sm_{1/7}Eu_{1/7}Dy_{1/7}Ho_{1/7}Yb_{1/7}Lu_{1/7}Ba_2Cu_3O_{7-\delta}$. At 20 K, the values for the different compounds are very similar, $\sim$2 MA/cm^2 independent of the number of *RE* [84]. Also, in 2023, the use of solid-state reaction synthesis has been continued. Suzuki et al. [86] followed this method to prepare HE *RE*BCO single-crystal whiskers with dimensions 0.5–1.0 mm in length, 10 μm in thickness, and 10–50 μm in width. The analytical HE *RE*BCO compositions were $Dy_{0.16}Ho_{0.17}Er_{0.20}Tm_{0.22}Yb_{0.25}Ba_2Cu_3O_{7-\delta}$, $Gd_{0.23}Dy_{0.17}Ho_{0.15}Er_{0.15}Tm_{0.19}Yb_{0.20}Ba_2Cu_3O_{7-\delta}$, and $Gd_{0.20}Dy_{0.13}Ho_{0.10}Er_{0.15}Tm_{0.09}Yb_{0.20}Lu_{0.15}Ba_2Cu_3O_{7-\delta}$. The T_c zero values of these compounds were around 89 K, which indicates that T_c of HE *RE*BCO compounds with a similar average *RE* ionic radius does not depend on the mixture entropy at the *RE* site. Therefore, the advantages of high-entropy alloys may be kept for a high degree of entropy without reducing the superconducting properties of the *RE*BCO compounds. Finally, Pryanichnikov et al. [91] synthesized equimolar $Y_{0.2}Nd_{0.2}Eu_{0.2}Sm_{0.2}Ho_{0.2}Ba_2Cu_3O_y$ bulk samples and studied their superconducting properties. The purpose of this work was to change the oxygen content by annealing in appropriate conditions and to study the crystal structure features and superconducting properties. It was concluded that *OP*, T_c, and J_c of $Y_{0.2}Nd_{0.2}Eu_{0.2}Sm_{0.2}Ho_{0.2}Ba_2Cu_3O_y$ increase with oxygen content y, very similar to their relatives of "low-entropy" *RE*BCO compounds.

Within the group of HE *RE*BCO compounds prepared as films, the first work published was the one of Yamashita et al., who prepared $Y_{0.12}Sm_{0.08}Eu_{0.26}Dy_{0.18}Ho_{0.36}Ba_2Cu_3O_{7-\delta}$ films by PLD [87]. This sample containing five *RE*s was compared with other low- and medium-entropy compounds. All samples grew with *c*-axis-preferential orientation. In addition, the *c*-axis of the samples increases with the average diameter of the *RE*s mixture and so does the width of the (005) peak, indicating, as expected, that there is an increase in the disorder of the crystal lattice. The T_c of the $Y_{0.12}Sm_{0.08}Eu_{0.26}Dy_{0.18}Ho_{0.36}Ba_2Cu_3O_{7-\delta}$ film was 90.5 K, the same as for the medium-entropy films with three and four *RE*s. It shows J_c = 2.3 MA/cm^2 at 4.2 K and 7 T, and that stays above 1.0 MA/cm^2 up to 20 K and 7 T. These values are very similar to the medium-entropy film with four *RE* and to the standard YBCO film in the high-field region. Few months later, Chen et al. reported the first HE *RE*BCO film deposited by fluorine-free CSD [88], namely, an 800-nm thick nominal $Y_{0.7}Gd_{0.2}Dy_{0.2}Sm_{0.2}Eu_{0.2}Ba_2Cu_3O_{7-\delta}$ film on technical substrates. This compound

presents the particularity that it was nominally off stoichiometry on the *RE* molarity because the authors argued this type of off-stoichiometric composition ratio provided better superconducting properties than standard 1:2:3, possibly mostly due to the formation of RE_2O_3 nanoparticles, which serve as pinning centers. The structural and superconducting properties of this HE *RE*BCO were compared with two control samples prepared the same way, $Y_1Dy_{0.5}Ba_2Cu_3O_{7-\delta}$ (also off stoichiometry on the *RE* molarity) and YBCO. They showed that high-quality *c*-axis-oriented $Y_{0.7}Gd_{0.2}Dy_{0.2}Sm_{0.2}Eu_{0.2}Ba_2Cu_3O_{7-\delta}$ films with T_c = 93 K can be obtained. The in-field J_c values of this HE *RE*BCO film are significantly improved, especially at 77 K or below 4 T. Self-field J_c values of 2, 4, and 10 MA/cm^2 were obtained at 77, 65, and 30 K, respectively. The maximum pinning force density of the HE *RE*BCO film at 77 K was 1.7 times higher than that of the standard YBCO film. However, it is difficult to confirm if this enhancement of J_c originates from the effect of the HE *RE* mixing or from the contribution of the RE_2O_3 pinning centers that were also found in the films. Fluorine-free solutions were also used by Masuda et al. to deposit 300-nm $Gd_{0.2}Sm_{0.2}Nd_{0.2}Eu_{0.2}Y_{0.2}Ba_2Cu_3O_{7-\delta}$ films on $LaAlO_3$ substrates [89]. The films show a T_c = 90.4 K and a self-field J_c = 2.4 MA/cm^2 at 77 K, both exceeding a standard GdBCO film of the same study. Cayado et al. raised the level of complexity further by introducing perovskite nanoparticles into the HE *RE*BCO film [90]. They prepared $Gd_{0.2}Dy_{0.2}Y_{0.2}Ho_{0.2}Er_{0.2}Ba_2Cu_3O_{7-\delta}$ nanocomposite films with 12 mol% $BaHfO_3$ (BHO) nanoparticles on $SrTiO_3$ substrates by CSD using full-TFA solutions. Both T_c and self-field J_c at 77 K of such a film, 91.9 K and 3.5 MA/cm^2, respectively, are comparable with the ones of low- and medium-entropy *RE*BCO films prepared in the same way. By an exhaustive TEM study, a homogeneous distribution of the BHO nanoparticles as well as a homogeneous distribution of the *RE*s at the atomic level instead of *RE* clustering, were observed, proving a true HE *RE*BCO. Grünewald et al. [92] of the same group continued these TEM analyses of such films, focusing on the mixing of *RE*s into the BHO nanoparticles. This is important as the possible incorporation of *RE*s in the nanoparticles could lead to off-stoichiometries in the *RE*BCO phase, causing a deviation from the expected growth process and reduction of the superconducting properties. The degree of *RE*s incorporation in BHO was found to depend on both the ionic radius and the content of the *RE*s in the *RE*BCO phase. The *RE*s incorporation increases with decreasing ionic radii and shows a stronger tendency for smaller ionic radii to intermix in medium- and high-entropy *RE*BCO than in the low-entropy ones.

4. Conclusion

In this comprehensive review, we have described the state of the art of superconducting high-entropy materials, focusing on fabrication methods and superconducting properties. The extension of high-entropy principles to the field of superconductivity has opened up new frontiers in the search for new superconductors and offers promising perspectives for innovative technological advancements. The potential applications of superconducting high-entropy materials cover a wide spectrum, from energy transmission to quantum computing. Their ability to maintain superconductivity under varying external conditions positions them as promising candidates for different applications. The discovery of new high-entropy superconductors has been continuous as the first one was found in 2014, while the interest in

this topic is growing year by year. Due to their chemical similarities, transition metals and rare earth elements are predestined for mixing on certain lattice sites. The first superconducting HE alloys contained only low transition metals, which were later extended to higher transition metals and even main group metals. These alloys with simple bcc crystal structures were further developed toward more complex crystal structures and further to compounds. In two layered compound classes, *RE*OBiS$_2$ and *RE*BCO, high-entropy mixing on the *RE* site has been shown. Similar investigations might be interesting in the iron-based superconducting *Ln*FeAsO system, *Ln* lanthanoid, which is still missing. Combining transition metal mixing and rare earth mixing on appropriate lattice sites might be a further increase in complexity. There is certainly still plenty of room for new, exciting investigations in this field.

Author details

Pablo Cayado[1]* and Jens Hänisch[2]

1 Department of Quantum Matter Physics (DQMP), University of Geneva, Geneva, Switzerland

2 Karlsruhe Institute of Technology (KIT), Institute for Technical Physics (ITEP), Eggenstein-Leopoldshafen, Germany

*Address all correspondence to: pablo.cayado@unige.ch

IntechOpen

References

[1] Yeh JW, Chen SK, Lin SJ, Gan JY, Chin TS, Shun TT, et al. Nanostructured high-entropy alloys with multiple principal elements: Novel alloy design concepts and outcomes. Advanced Engineering Materials. 2004;**6**(5):299-303

[2] Cantor B, Chang ITH, Knight P, Vincent AJB. Microstructural development in equiatomic multicomponent alloys. Materials Science and Engineering: A. 2004;**375–377**(1-2 Spec. issue):213-218

[3] Yuan Y, Wu Y, Luo H, Wang Z, Liang X, Yang Z, et al. Superconducting Ti15Zr15Nb35Ta35 high-entropy alloy with intermediate electron-phonon coupling. Frontiers in Materials. 2018;**5**

[4] Sun L, Cava RJ. High-entropy alloy superconductors: Status, opportunities, and challenges. Physical Review Materials. 2019;**3**(9):090301

[5] Koželj P, Vrtnik S, Jelen A, Jazbec S, Jagličić Z, Maiti S, et al. Discovery of a superconducting high-entropy alloy. Physical Review Letters. 2014;**113**(10):107001

[6] Matthias BT. Empirical relation between superconductivity and the number of valence electrons per atom. Physical Review. 1955;**97**:74

[7] Wu J, Liu B, Cui Y, Zhu Q, Xiao G, Wang H, et al. Polymorphism and superconductivity in the V-Nb-Mo-Al-Ga high-entropy alloys. Science China Materials. 2020;**63**(5):823-831

[8] Liu B, Wu J, Cui Y, Zhu Q, Xiao G, Wang H, et al. Formation and superconductivity of single-phase high-entropy alloys with a tetragonal structure. ACS Applied Electronic Materials. 2020;**2**(4):1130-1137

[9] Senkov ON, Scott JM, Senkova SV, Miracle DB, Woodward CF. Microstructure and room temperature properties of a high-entropy TaNbHfZrTi alloy. Journal of Alloys and Compounds. 2011;**509**(20):6043-6048

[10] Shukunami Y, Yamashita A, Goto Y, Mizuguchi Y. Synthesis of RE123 high-Tc superconductors with a high-entropy-alloy-type RE site. Physica C: Superconductivity and Its Applications. 2020;**572**:1353623

[11] Jasiewicz K, Wiendlocha B, Korbeń P, Kaprzyk S, Tobola J. Superconductivity of Ta34Nb33Hf8Zr14Ti11 high entropy alloy from first principles calculations. Physica Status Solidi (RRL)–Rapid Research Letters. 2016;**10**(5):415-419

[12] Vrtnik S, Koželj P, Meden A, Maiti S, Steurer W, Feuerbacher M, et al. Superconductivity in thermally annealed Ta-Nb-Hf-Zr-Ti high-entropy alloys. Journal of Alloys and Compounds. 2017;**695**:3530-3540

[13] Von Rohr F, Winiarski MJ, Tao J, Klimczuk T, Cava RJ. Effect of electron count and chemical complexity in the Ta-Nb-Hf-Zr-Ti high-entropy alloy superconductor. Proceedings of the National Academy of Sciences. 2016;**113**(46):E7144-E7150

[14] Guo J, Wang H, Von Rohr F, Wang Z, Cai S, Zhou Y, et al. Robust zero resistance in a superconducting high-entropy alloy at pressures up to 190 GPa. Proceedings of the National Academy of Sciences. 2017;**114**(50):13144-13147

[15] Wu KY, Chen SK, Wu JM. Superconducting in equal molar NbTaTiZr-based high-entropy alloys. Natural Science. 2018;**10**(03):110

[16] Kim G, Lee MH, Yun JH, Rawat P, Jung SG, Choi W, et al. Strongly correlated and strongly coupled s-wave superconductivity of the high entropy alloy Ta1/6Nb2/6Hf1/6Zr1/6Ti1/6 compound. Acta Materialia. 2020;**186**: 250-256

[17] Kim J, Jung SG, Han Y, Kim JH, Rhyee JS, Yeo S, et al. Thermal-driven gigantic enhancement in critical current density of high-entropy alloy superconductors. Journal of Materials Science and Technology. 2024;**189**:60-67

[18] Idczak R, Nowak W, Rusin B, Topolnicki R, Ossowski T, Babij M, et al. Enhanced superconducting critical parameters in a new high-entropy alloy Nb0.34Ti0.33Zr0.14Ta0.11Hf0.08. Materials. 2023;**16**(17):5814

[19] Jasiewicz K, Wiendlocha B, Górnicka K, Gofryk K, Gazda M, Klimczuk T, et al. Pressure effects on the electronic structure and superconductivity of (TaNb)0.67(HfZrTi)0.33 high entropy alloy. Physical Review B. 2019;**100**(18): 184503

[20] Horvat J, Soltanian S, Pan AV, Wang XL. Superconducting screening on different length scales in high-quality bulk MgB2 superconductor. Journal of Applied Physics. 2004;**96**(8):4342-4351

[21] Kim JH, Hidayati R, Jung SG, Salawu YA, Kim HJ, Yun JH, et al. Enhancement of critical current density and strong vortex pinning in high entropy alloy superconductor Ta1/6Nb2/6Hf1/6Zr1/6Ti1/6 synthesized by spark plasma sintering. Acta Materialia. 2022;**232**: 117971

[22] Hong VTA, Jang H, Jung SG, Han Y, Kim JH, Hidayati R, et al. Probing superconducting gap of the high-entropy alloy Ta1/6Nb2/6Hf1/6Zr1/6Ti1/6 via

Andreev reflection spectroscopy. Physical Review B. 2022;**106**(2):024504

[23] Jung SG, Han Y, Kim JH, Hidayati R, Rhyee JS, Lee JM, et al. High critical current density and high-tolerance superconductivity in high-entropy alloy thin films. Nature Communications. 2022;**13**(1):3373

[24] Zhang X, Winter N, Witteveen C, Moehl T, Xiao Y, Krogh F, et al. Preparation and characterization of high-entropy alloy (TaNb)1−x(ZrHfTi) x superconducting films. Physical Review Research. 2020;**2**(1):013375

[25] Pristáš G, Bačkai J, Orendáč M, Gabáni S, Košuth F, Kuzmiak M, et al. Superconductivity in medium-and high-entropy alloy thin films: Impact of thickness and external pressure. Physical Review B. 2023;**107**(2):024505

[26] Shu R, Zhang X, Rao SG, Le Febvrier A, Eklund P. Effects of alloying and deposition temperature on phase formation and superconducting properties of TiZrTaNb-based high entropy-alloy films. Applied Physics Letters. 2022;**120**(15):151901

[27] Marik S, Varghese M, Sajilesh KP, Singh D, Singh RP. Superconductivity in equimolar Nb-Re-Hf-Zr-Ti high entropy alloy. Journal of Alloys and Compounds. 2018;**769**:1059-1063

[28] Motla K, Meena PK, Singh D, Biswas PK, Hillier AD, Singh RP. Superconducting and normal-state properties of the high-entropy alloy Nb-Re-Hf-Zr-Ti investigated by muon spin relaxation and rotation. Physical Review B. 2022;**105**(14):144501

[29] Hattori T, Watanabe Y, Nishizaki T, Hiraoka K, Kakihara M, Hoshi K, et al. Metallurgy, superconductivity, and hardness of a new high-entropy alloy

superconductor Ti-Hf-Nb-Ta-Re. Journal of Alloys and Metallurgical Systems. 2023;**3**:100020

[30] Kitagawa J, Hoshi K, Kawasaki Y, Koga R, Mizuguchi Y, Nishizaki T. Superconductivity and hardness of the equiatomic high-entropy alloy HfMoNbTiZr. Journal of Alloys and Compounds. 2022;**924**:166473

[31] Zeng L, Zhan J, Boubeche M, Li K, Li L, Yu P, et al. Superconductivity in the bcc-type high-entropy alloy TiHfNbTaMo. Advanced Quantum Technologies. 2023;**6**:2300213

[32] Sobota P, Topolnicki R, Ossowski T, Pikula T, Pikul A, Idczak R. Superconductivity in the high-entropy alloy (NbTa)0.67(MoHfW)0.33. Physical Review B. 2022;**106**(18)

[33] Ishizu N, Kitagawa J. New high-entropy alloy superconductor Hf21Nb25Ti15V15Zr24. Results in Physics. 2019;**13**:102275

[34] Sarkar NK, Prajapat CL, Ghosh PS, Garg N, Babu PD, Wajhal S, et al. Investigations on superconductivity in an equi-atomic disordered Hf-Nb-Ta-Ti-V high entropy alloy. Intermetallics (Barking). 2022;**144**:107503

[35] Nelson WL, Chemey AT, Hertz M, Choi E, Graf DE, Latturner S, et al. Superconductivity in a uranium containing high entropy alloy. Scientific Reports. 2020;**10**(1):4717

[36] Von Rohr FO, Cava RJ. Isoelectronic substitutions and aluminium alloying in the Ta-Nb-Hf-Zr-Ti high-entropy alloy superconductor. Physical Review Materials. 2018;**2**(3):034801

[37] Krnel M, Jelen A, Vrtnik S, Luzar J, Gačnik D, Koželj P, et al. The effect of scandium on the structure,

microstructure and superconductivity of equimolar Sc-Hf-Nb-Ta-Ti-Zr refractory high-entropy alloys. Materials. 2022;**15**(3):1122

[38] Harayama Y, Kitagawa J. Superconductivity in Al-Nb-Ti-V-Zr multicomponent alloy. Journal of Superconductivity and Novel Magnetism. 2021;**34**(11):2787-2794

[39] Zherebtsov S, Yurchenko N, Panina E, Tikhonovsky M, Stepanov N. Gum-like mechanical behavior of a partially ordered Al5Nb24Ti40V5Zr26 high entropy alloy. Intermetallics (Barking). 2020;**116**:106652

[40] Zhang X, Eklund P, Shu R. Superconductivity in (TaNb)1-x(ZrHfTi)xMoy high-entropy alloy films. Applied Physics Letters. 2023;**123**(5):051902

[41] Stolze K, Tao J, Von Rohr FO, Kong T, Cava RJ. Sc–Zr–Nb–Rh–Pd and Sc–Zr–Nb–Ta–Rh–Pd high-entropy alloy superconductors on a CsCl-type lattice. Chemistry of Materials. 2018;**30**(3):906-914

[42] Pan Y, He X, Zhou B, Strong D, Zhang J, Bin YH, et al. Elastic properties of a Sc–Zr–Nb–Ta–Rh–Pd high-entropy alloy superconductor. Materials Today Communications. 2022;**33**:104265

[43] Stolze K, Cevallos FA, Kong T, Cava RJ. High-entropy alloy superconductors on an α-Mn lattice. Journal of Materials Chemistry C. 2018;**6**(39):10441-10449

[44] Liu B, Wu J, Cui Y, Zhu Q, Xiao G, Wu S, et al. Structural evolution and superconductivity tuned by valence electron concentration in the Nb-Mo-Re-Ru-Rh high-entropy alloys. Journal of Materials Science and Technology. 2021;**85**:11-17

[45] Marik S, Motla K, Varghese M, Sajilesh KP, Singh D, Breard Y, et al. Superconductivity in a new hexagonal high-entropy alloy. Physical Review Materials. 2019;**3**(6):060602

[46] Lee YS, Cava RJ. Superconductivity in high and medium entropy alloys based on MoReRu. Physica C: Superconductivity and its Applications. 2019;**566**:1353520

[47] Liu B, Wu J, Cui Y, Zhu Q, Xiao G, Wu S, et al. Superconductivity in hexagonal Nb-Mo-Ru-Rh-Pd high-entropy alloys. Scripta Materialia. 2020;**182**:109-113

[48] Hirai D, Uematsu N, Saitoh K, Katayama N, Takenaka K. Superconductivity in high-entropy antimonide M1–x Pt x Sb (M = equimolar Ru, Rh, Pd, and Ir). Inorganic Chemistry. 2023;**62**(35):14207-14215

[49] Zhu Q, Xiao G, Cui Y, Yang W, Song S, Cao GH, et al. Structural transformation and superconductivity in carbon-added hexagonal high-entropy alloys. Journal of Alloys and Compounds. 2022;**909**:164700

[50] Liu B, Wu J, Cui Y, Zhu Q, Xiao G, Wu S, et al. Superconductivity and paramagnetism in Cr-containing tetragonal high-entropy alloys. Journal of Alloys and Compounds. 2021;**869**: 159293

[51] Xiao G, Zhu Q, Yang W, Cui Y, Song S, Cao GH, et al. Centrosymmetric to noncentrosymmetric structural transformation in a superconducting high-entropy alloy due to carbon addition. Science China Materials. 2023; **66**(1):257-263

[52] Xiao G, Yang W, Zhu Q, Song S, Cao GH, Ren Z. Superconductivity with large upper critical field in

noncentrosymmetric Cr-bearing high-entropy alloys. Scripta Materialia. 2023; **223**:115099

[53] Motla K, Soni V, Meena PK, Singh RP. Boron based new high entropy alloy superconductor Mo0.11W0.11V0.11Re0.34B0.33. Superconductor Science and Technology. 2022;**35**(7):074002

[54] Kasem MR, Yamashita A, Goto Y, Matsuda TD, Mizuguchi Y. Synthesis of high-entropy-alloy-type superconductors (Fe,Co,Ni,Rh,Ir)Zr2 with tunable transition temperature. Journal of Materials Science. 2021;**56** (15):9499-9505

[55] Liu B, Wu J, Cui Y, Zhu Q, Xiao G, Wu S, et al. Superconductivity in cubic A15-type V–Nb–Mo–Ir–Pt high-entropy alloys. Frontiers of Physics. 2021;**9**

[56] Yamashita A, Matsuda TD, Mizuguchi Y. Synthesis of new high-entropy alloy-type Nb3 (Al, Sn, Ge, Ga, Si) superconductors. Journal of Alloys and Compounds. 2021;**868**:159233

[57] Nakahira Y, Kiyama R, Yamashita A, Itou H, Miura A, Moriyoshi C, et al. Tuning of upper critical field in a vanadium-based A15 superconductor by the compositionally-complex-alloy concept. Journal of Materials Science. 2022;**6**:15990-15998

[58] Mizuguchi Y, Kasem MR, Matsuda TD. Superconductivity in CuAl2-type Co0.2Ni0.1Cu0.1Rh0.3Ir0.3Zr2 with a high-entropy-alloy transition metal site. Materials Research Letters. 2021;**9**(3): 141-147

[59] Kasem MR, Yamashita A, Hatano T, Sakurai K, Oono-Hori N, Goto Y, et al. Anomalous broadening of specific heat jump at Tc in high-entropy-alloy-type

superconductor TrZr2. Superconductor Science and Technology. 2021;**34**:125001

[60] Pugliese GM, Tortora L, Tomassucci G, Kasem RM, Mizokawa T, Mizuguchi Y, et al. Possible local order in the high entropy TrZr2 superconductors. Journal of Physics and Chemistry of Solids. 2023;**174**:111154

[61] Fujita Y, Kinami K, Hanada Y, Nagao M, Miura A, Hirai S, et al. Growth and characterization of ROBiS2 high-entropy superconducting single crystals. ACS Omega. 2020;**5**(27):16819-16825

[62] Zeng L, Wang Z, Song J, Lin G, Guo R, Luo SC, et al. Discovery of the high-entropy carbide ceramic topological superconductor candidate (Ti0.2Zr0.2Nb0.2Hf0.2Ta0.2)C. Advanced Functional Materials. 2023;**33**:2301929

[63] Shu H, Zhong W, Feng J, Zhao H, Yue B. Coexistence of superconductivity and ferromagnetism in high entropy carbide ceramics. arXiv:2307.16438

[64] Mizuguchi Y. Superconductivity in high-entropy-alloy telluride AgInSnPbBiTe5. Journal of the Physical Society of Japan. 2019;**88**:124708

[65] Kasem MR, Ishii R, Katase T, Miura O, Mizuguchi Y. Tuning of carrier concentration and superconductivity in high-entropy-alloy-type metal telluride (AgSnPbBi)(1-x)/4InxTe. Journal of Alloys and Compounds. 2022;**920**:166013

[66] Ying T, Yu T, Shiah YS, Li C, Li J, Qi Y, et al. High-entropy van der Waals materials formed from mixed metal dichalcogenides, halides, and phosphorus trisulfides. Journal of the American Chemical Society. 2021;**143**(18):7042-7049

[67] Liu B, Yang W, Xiao G, Zhu Q, Song S, Cao GH, et al. High-entropy silicide superconductors with W5Si3-type structure. Physical Review Materials. 2023;**7**:014805

[68] Sogabe R, Goto Y, Mizuguchi Y. Superconductivity in REO0.5F0.5BiS2 with high-entropy-alloy-type blocking layers. Applied Physics Express. 2018;**11**:053102

[69] Sogabe R, Goto Y, Abe T, Moriyoshi C, Kuroiwa Y, Miura A, et al. Improvement of superconducting properties by high mixing entropy at blocking layers in BiS2 -based superconductor REO0.5F0.5BiS2. Solid State Communications. 2019;**295**:43-49

[70] Fujita Y, Nagao M, Miura A, Urushihara D, Mizuguchi Y, Maruyama Y, et al. Effects of equivalent composition on superconducting properties of high-entropy REOBiS2 (RE = La, Ce, Pr, Nd, Sm, Gd) single crystals. Physica C: Superconductivity and its Applications. 2023;**608**:1354254

[71] Rost CM, Sachet E, Borman T, Moballegh A, Dickey EC, Hou D, et al. Entropy-stabilized oxides. Nature Communications. 2015;**6**(1):8485

[72] Oses C, Toher C, Curtarolo S. High-entropy ceramics. Nature Reviews Materials. Nature Research. 2020;**5**:295-309

[73] Akrami S, Edalati P, Fuji M, Edalati K. High-entropy ceramics: Review of principles, production and applications. Materials Science and Engineering R. 2021;**146**:100644

[74] Zhang RZ, Reece MJ. Review of high entropy ceramics: Design, synthesis, structure and properties. Journal of Materials Chemistry A. Royal Society of Chemistry. 2019;**7**:22148-22162

[75] Zhang J, Xu B, Xiong Y, Ma S, Wang Z, Wu Z, et al. Design high-entropy carbide ceramics from machine learning. npj Computational Materials. 2022;**8**(1):5

[76] Kasem MR, Nakahira Y, Yamaoka H, Matsumoto R, Yamashita A, Ishii H, et al. Robustness of superconductivity to external pressure in high-entropy-alloy-type metal telluride AgInSnPbBiTe5. Scientific Reports. 2022;**12**:7789

[77] Mizuguchi Y, Demura S, Deguchi K, Takano Y, Fujihisa H, Gotoh Y, et al. Superconductivity in novel BiS 2-based layered superconductor LaO1-xFxBiS2. Journal of the Physical Society of Japan. 2012;**81**:114725

[78] Bérardan D, Franger S, Dragoe D, Meena AK, Dragoe N. Colossal dielectric constant in high entropy oxides. Physica Status Solidi - Rapid Research Letters. 2016;**10**(4):328-333

[79] Sarkar A, Wang Q, Schiele A, Chellali MR, Bhattacharya SS, Wang D, et al. High-entropy oxides: Fundamental aspects and electrochemical properties. Advanced Materials. 2019;**31**:1806236

[80] Li H, Zhou Y, Liang Z, Ning H, Fu X, Xu Z, et al. High-entropy oxides: Advanced research on electrical properties. Coatings. 2021;**11**:628

[81] Brahlek M, Gazda M, Keppens V, Mazza AR, McCormack SJ, Mielewczyk-Gryń A, et al. What is in a name: Defining 'high entropy' oxides. APL Materials. 2022;**10**:110902

[82] Aamlid SS, Oudah M, Rottler J, Hallas AM. Understanding the role of entropy in high entropy oxides. Journal of the American Chemical Society. American Chemical Society. 2023;**145**: 5991-6006

[83] Mazza AR, Gao X, Rossi DJ, Musico BL, Valentine TW, Kennedy Z, et al.

Searching for superconductivity in high entropy oxide Ruddlesden–Popper cuprate films. Journal of Vacuum Science & Technology A. 2022;**40**: 013404

[84] Wang K, Hou Q, Pal A, Wu H, Si J, Chen J, et al. Structural and physical properties of high-entropy REBa2Cu3O7-δ oxide superconductors. Journal of Superconductivity and Novel Magnetism. 2021;**34**(5):1379-1385

[85] Yamashita A, Shukunami Y, Mizuguchi Y. Improvement of critical current density of RE Ba2Cu3O7-δ by increase in configurational entropy of mixing. Royal Society Open Science. 2022;**9**(3):211874

[86] Suzuki Y, Nagao M, Maruyama Y, Watauchi S, Tanaka I. Growth of REBa2Cu3Ox single-crystal whiskers utilizing the concept of high-entropy alloys. Japanese Journal of Applied Physics. 2023;**62**:033001

[87] Yamashita A, Hashimoto K, Suzuki S, Nakanishi Y, Miyata Y, Maeda T, et al. Fabrication of high-entropy REBa2Cu3O7− δ thin films by pulsed laser deposition. Japanese Journal of Applied Physics. 2022;**61**(5):050905

[88] Chen J, Huang R, Zhou X, Zhou D, Li M, Bai C, et al. Nucleation and epitaxy growth of high-entropy REBa2Cu3O7–δ (RE= Y, Dy, Gd, Sm, Eu) thin films by metal organic deposition. Journal of Rare Earths. 2023;**41**(7):1091-1098

[89] Masuda H, Ishii R, Kita R, Miura O. Superconducting properties of high-entropy type RE123 thin films by fluorine-free MOD method. IEEE Transactions on Applied Superconductivity. 2023;**33**(5):7200203

[90] Cayado P, Grünewald L, Erbe M, Hänisch J, Gerthsen D, Holzapfel B.

Critical current density improvement in CSD-grown high-entropy REBa2Cu3O7−δ films. RSC Advances. 2022;**12**(44):28831-28842

[91] Pryanichnikov S, Vidmid' L, Titova S. High-entropy superconducting oxides (Y,Nd,Eu,Sm,Ho)Ba2Cu3Oy with different oxygen contents. Journal of Superconductivity and Novel Magnetism. 2023;**36**(3):871-875

[92] Grünewald L, Cayado P, Erbe M, Hänisch J, Holzapfel B, Gerthsen D. Analytical electron microscopy study of the composition of $BaHfO_3$ nanoparticles in REBCO films: The influence of rare-earth ionic radii and REBCO composition. Materials Advances. 2023; **4**:6507-6521